1
Principles of X-ray Diffraction

Diffraction effects are observed when electromagnetic radiation impinges on periodic structures with geometrical variations on the length scale of the wavelength of the radiation. The interatomic distances in crystals and molecules amount to 0.15–0.4 nm which correspond in the electromagnetic spectrum with the wavelength of x-rays having photon energies between 3 and 8 keV. Accordingly, phenomena like constructive and destructive interference should become observable when crystalline and molecular structures are exposed to x-rays.

In the following sections, firstly, the geometrical constraints that have to be obeyed for x-ray interference to be observed are introduced. Secondly, the results are exemplified by introducing the $\theta/2\theta$ scan, which is a major x-ray scattering technique in thin-film analysis. Thirdly, the $\theta/2\theta$ diffraction pattern is used to outline the factors that determine the intensity of x-ray reflections. We will thereby rely on numerous analogies to classical optics and frequently use will be made of the fact that the scattering of radiation has to proceed coherently, i.e. the phase information has to be sustained for an interference to be observed.

In addition, the three coordinate systems as related to the crystal $\{\boldsymbol{c}_i\}$, to the sample or specimen $\{\boldsymbol{s}_i\}$ and to the laboratory $\{\boldsymbol{l}_i\}$ that have to be considered in diffraction are introduced. Two instrumental sections (Instrumental Boxes 1 and 2) related to the $\theta/2\theta$ diffractometer and the generation of x-rays by x-ray tubes supplement the chapter. One-elemental metals and thin films composed of them will serve as the material systems for which the derived principles are demonstrated. A brief presentation of one-elemental structures is given in Structure Box 1.

1.1
The Basic Phenomenon

Before the geometrical constraints for x-ray interference are derived the interactions between x-rays and matter have to be considered. There are three different types of interaction in the relevant energy range. In the first, electrons may be liberated from their bound atomic states in the process of photoionization. Since energy and momentum are transferred from the incoming radiation to the excited electron, photoionization falls into the group of inelastic scattering processes. In

Thin Film Analysis by X-Ray Scattering. M. Birkholz
Copyright © 2006 WILEY-VCH Verlag GmbH & Co. KGaA, Weinheim
ISBN: 3-527-31052-5

COPYRIGHTED MATERIAL

addition, there exists a second kind of inelastic scattering that the incoming x-ray beams may undergo, which is termed Compton scattering. Also in this process energy is transferred to an electron, which proceeds, however, without releasing the electron from the atom. Finally, x-rays may be scattered elastically by electrons, which is named Thomson scattering. In this latter process the electron oscillates like a Hertz dipole at the frequency of the incoming beam and becomes a source of dipole radiation. The wavelength λ of x-rays is conserved for Thomson scattering in contrast to the two inelastic scattering processes mentioned above. It is the Thomson component in the scattering of x-rays that is made use of in structural investigations by x-ray diffraction.

Figure 1.1 illustrates the process of elastic scattering for a single free electron of charge e, mass m and at position $\boldsymbol{R_0}$. The incoming beam is accounted for by a plane wave $\boldsymbol{E_0}\exp(-i\boldsymbol{K_0}\boldsymbol{R_0})$, where $\boldsymbol{E_0}$ is the electrical field vector and $\boldsymbol{K_0}$ the wave vector. The dependence of the field on time will be neglected throughout. The wave vectors $\boldsymbol{K_0}$ and $\boldsymbol{K}$ describe the direction of the incoming and exiting beam and both are of magnitude $2\pi/\lambda$. They play an important role in the geometry of the scattering process and the plane defined by them is denoted as the scattering plane. The angle between $\boldsymbol{K}$ and the prolonged direction of $\boldsymbol{K_0}$ is the scattering angle that will be abbreviated by 2θ as is general use in x-ray diffraction. We may also define it by the two wave vectors according to

$$2\theta = \arccos\frac{\langle \boldsymbol{K}, \boldsymbol{K}_0 \rangle}{KK_0} \tag{1.1}$$

The formula is explicitly given here, because the definition of angles by two adjoining vectors will be made use of frequently.

The oscillating charge e will emit radiation of the same wavelength λ as the primary beam. In fact, a phase shift of 180° occurs with the scattering, but since this shift equally arises for every scattered wave it has no effect on the interference pattern in which we are interested and will be neglected. If the amplitude of the scattered wave $\boldsymbol{E}(\boldsymbol{R})$ is considered at a distance $\boldsymbol{R}$ we may write according to Hertz and Thomson

$$\boldsymbol{E}(\boldsymbol{R}) = \boldsymbol{E}_0 \frac{1}{4\pi\varepsilon_0 R}\frac{e^2}{mc^2}\sin\angle(\boldsymbol{E}_0, \boldsymbol{R})\exp(-i\boldsymbol{K}\boldsymbol{R}) \tag{1.2}$$

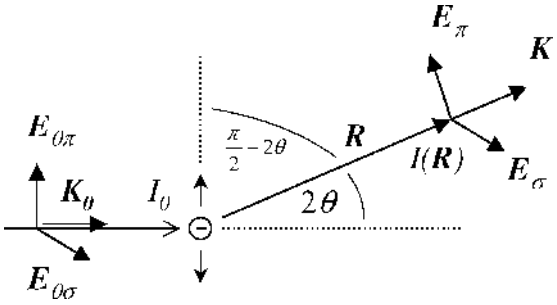


Figure 1.1 Scattering of x-rays by a single electron.

where ε_0 and c are the vacuum permittivity and velocity of light. The field vector $\boldsymbol{E}$ and wave vector $\boldsymbol{K}$ are oriented perpendicular to each other as is usual for electromagnetic waves. The sin term is of significance when the state of polarization is considered for which two extreme cases may arise. In one case, the exciting field $\boldsymbol{E_0}$ is confined to the scattering plane and in the second case it is normally oriented. In classical optics these two cases are named π polarization and σ polarization. The field vectors in both cases will be denoted by $\boldsymbol{E}_\pi$ and $\boldsymbol{E}_\sigma$. The angle between $\boldsymbol{E}_\sigma$ and $\boldsymbol{R}$ is always 90° and the sin term will equal unity. For the case of π polarization, however, it may be expressed by virtue of the scattering angle according to $\sin\angle(\boldsymbol{E_0}, \boldsymbol{R}) = |\cos 2\theta|$. If the character C abbreviates the sin term it may be written

$$C = \begin{cases} 1 & \sigma\text{-polarization} \\ |\cos 2\theta| & \pi\text{-polarization} \end{cases} \tag{1.3}$$

Since the intensity is obtained from the sum of the square of both field vectors the expression

$$\left(\frac{1}{4\pi\varepsilon_0 R}\right)^2 \left(\frac{e^2}{mc^2}\right)^2 \left(E_\sigma^2 + E_\pi^2 \cos^2 2\theta\right) \tag{1.4}$$

is obtained. In a nonpolarized beam both polarization states will have the same probability of occurring,

$$\overline{E_\sigma^2} = \overline{E_\pi^2} = I_0 / 2$$

and it is finally arrived at the intensity of the scattered beam at distance R

$$I(\boldsymbol{R}) = I_0 \frac{r_e^2}{R^2} \frac{1 + \cos^2 2\theta}{2} \tag{1.5}$$

Here, use has been made of the notion of the classical radius of the electron, $r_e = e^2/(4\pi\varepsilon_0 mc^2)$, that amounts to 2.82×10^{-15} m. The intensity of the scattering is seen to scale with the inverse of R^2 as might have been expected. It can also be seen that $I(\boldsymbol{R})$ scales with the ratio of squares of r_e over R. Since distances R of the order of 10^{-1} m are realized in typical laboratory setups the probability of observing the scattering by a single electron tends to zero. The situation substantially improves if the number of scattering objects is of the same order of magnitude as Loschmidt's number N_L – as usually is the case in experiments.

It also becomes evident from this equation as to why the scattering from atomic nuclei has not been considered in the derivation. In fact, the equation would also hold for the scattering from atomic nuclei, but it can be seen from Eq. (1.4) that the nuclei component will only yield a less than 10^{-6} smaller intensity compared to an electron. The difference is simply due to the mass difference, which is at least larger by a factor of 1836 for any atomic species. The scattering of x-rays by nuclei may, therefore, confidently be neglected. From the viewpoint of x-ray scattering an atom can thus be modeled by the number of Z electrons, which it contains according to its rank in the periodic table. In terms of the Thompson scattering model Zr_e may be written in Eq. (1.3) instead of r_e in order to describe the scattering from an atom,

since the primary beam is then equally scattered by all electrons. In addition, it will be assumed temporarily that all electrons are confined to the origin of the atom. The consequences that follow from a refinement of the model by assuming a spatially extended charge distribution will be postponed to a later section. Hence, we have a first quantitative description for the x-ray elastic scattering from an atom.

In the next step consideration is given to what the scattering will look like if it occurs for a whole group of atoms that are arranged in a periodically ordered array like a crystal lattice. Figure 1.2 visualizes such an experiment where the crystal is irradiated with monochromatic x-rays of wavelength λ. In the special case considered here, each atom is surrounded by six neighbor atoms at distance a and the angle between two atomic bonds is always 90° or multiples of it. Atomic positions can then be described by the lattice vector $\boldsymbol{r}_{n_1n_2n_3} = n_1a\boldsymbol{c}_1 + n_2a\boldsymbol{c}_2 + n_3a\boldsymbol{c}_3$ with $\boldsymbol{c}_1$, $\boldsymbol{c}_2$ and $\boldsymbol{c}_3$ being the unit vectors of the three orthogonal directions in space. The $\boldsymbol{c}_i$ axes are the unit vectors of the crystal coordinate system $\{\boldsymbol{c}_i\}$, which is assigned to the crystal. For some properties of the crystal this coordinate system will turn out to be extremely useful and the notion will be used throughout the book. The shape of the crystal is assumed to be that of a parallelepiped as is accounted for by the inequalities $0 \le n_i = N_i - 1$ for $i = 1, 2, 3$. Each node of adjacent cubes is thus occupied by an atom. Such a structure is called simple cubic in crystallography. Only a single element crystallizes in this structure, which is polonium exhibiting an interatomic distance of $a = 0.3359$ nm. Although this metal has only very few applications, the case shall be considered here in detail, because of its clarity and simplicity.

It will now be calculated at which points in space interferences of x-rays might be observed that arise due to the scattering at the crystal lattice. The task is to quantify the strength of the scattered fields at a point $\boldsymbol{R}$ when elastic scattering occurs according to Eq. (1.5) at all atoms. The reference point of $\boldsymbol{R}$ is chosen such that it starts at the origin of the crystal lattice $\boldsymbol{r}_{000}$. This means that we relate the phase difference in the summation of all scattered fields to their phase at $\boldsymbol{r}_{000}$. This choice is arbitrary and any other lattice point might have been equally selected.

The wave vector of the primary beam $\boldsymbol{K}_0$ is assumed to be parallel to the [100] direction of the crystal. The scattering plane defined by $\boldsymbol{K}_0$ and $\boldsymbol{K}$ may coincide with one of the (010) planes. The wavefronts of the incoming plane waves which are the planes of constant phase are then oriented parallel to (100) planes. An atom on the position $\boldsymbol{r}_{n_1n_2n_3}$ would then cause a scattering intensity to be measured at $\boldsymbol{R}$ of the strength

$$E_0 \exp(-i\boldsymbol{K}_0\boldsymbol{r}_{n_1n_2n_3}) \frac{Zr_e}{\left|\boldsymbol{R} - \boldsymbol{r}_{n_1n_2n_3}\right|} \sin\angle(\boldsymbol{E}_0, \boldsymbol{R} - \boldsymbol{r}_{n_1n_2n_3}) \exp(-i\boldsymbol{K}(\boldsymbol{R} - \boldsymbol{r}_{n_1n_2n_3})) \qquad (1.6)$$

This expression differs from Eq. (1.2) essentially by the fact that $\boldsymbol{R} - \boldsymbol{r}_{n_1n_2n_3}$ occurs instead of $\boldsymbol{R}$, and for $n_1 = n_2 = n_3 = 0$ it becomes equal to Eq. (1.2). The solution of our task would simply consist in a summation over all fields scattered by the number of $N_1 \times N_2 \times N_3$ atoms comprising the crystal. However, the physics of the solution will become more transparent when an important approximation is made.

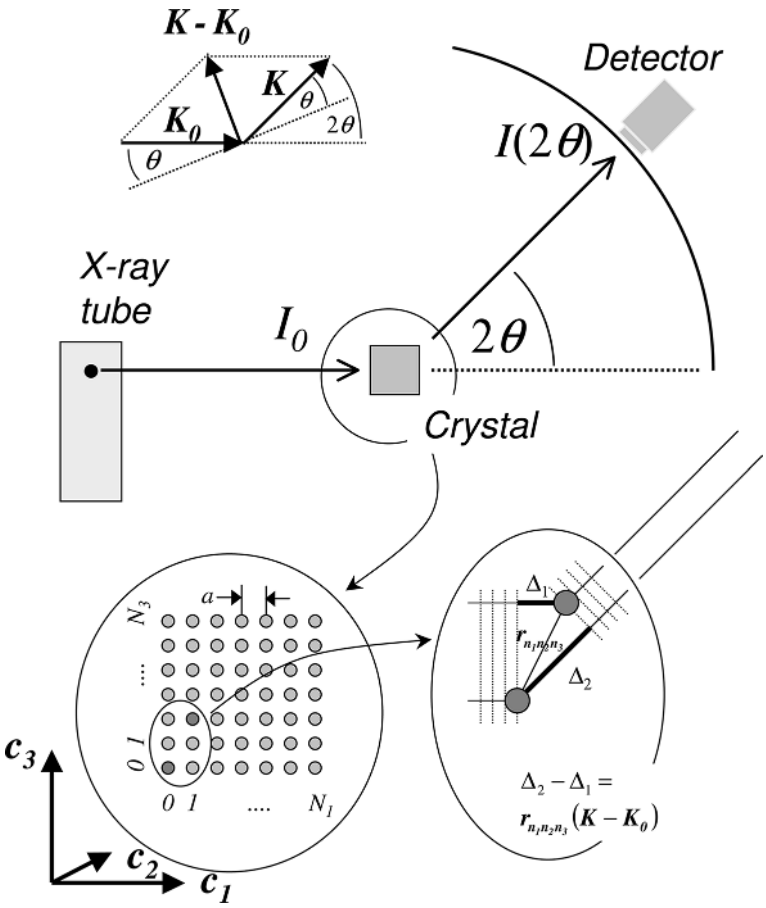


Figure 1.2 Scattering of x-rays by a crystallite of simple cubic structure.

It will be assumed that the interatomic distances r_{n1n2n3} (~10^{-10} m) are much smaller than the distances to the point of the intensity measurement $R - r_{n1n2n3}$ (~10^{-1} m). The denominator in Eq. (1.6) and in the sin term $\boldsymbol{R} - \boldsymbol{r}_{n_1n_2n_3}$ may then be replaced by $\boldsymbol{R}$ without introducing a large error. This substitution, however, is not allowed in the exponent of the last factor, since the interatomic distances are of the order of the wavelength and every phase shift according $\boldsymbol{K}\boldsymbol{r}_{n_1n_2n_3} = 2\pi r_{n1n2n3}/\lambda$ has to be fully taken into account in the summation procedure. If these rules are applied the sin term may be replaced by the polarization factor C and the sum over all scattered fields reads

$$\boldsymbol{E}_0 \frac{Zr_e}{R} C \exp\left(-i\boldsymbol{K}\boldsymbol{R}\right) \sum_{n_1n_2n_3} \exp\left(-i(\boldsymbol{K} - \boldsymbol{K}_0)\boldsymbol{r}_{n_1n_2n_3}\right) \tag{1.7}$$

All terms independent of the lattice vector $\boldsymbol{r}_{n_1n_2n_3}$ could be placed in front of the summation symbol. The approximation of which we have made use of is named Fraunhofer diffraction, which is always a useful approach when the distances between scattering objects are much smaller than the distance to the measurement point. In contrast to this approach stands the so-called Fresnel diffraction, for which interference phenomena are investigated very close to the scattering objects. The case of Fresnel diffraction will not be of interest here.

We have achieved a significant progress in solving our task by applying the Fraunhofer approximation and arriving at Eq. (1.7). It can be seen that the scattered field scales with two factors, where the first has the appearance of a spherical wave while the second is a sum over exponentials of vector products of wave vectors and lattice vectors. In order to improve our understanding of the summation over so many scattering centers the geometry is shown in the lower part of Fig. 1.2. A closer look at the figure reveals that the phase shift for two waves (a) scattered at $\boldsymbol{r}_{000}$ and (b) scattered at $\boldsymbol{r}_{n_1n_2n_3}$ comprises two components due to $\boldsymbol{K}_0\boldsymbol{r}_{n_1n_2n_3}$ and to $\boldsymbol{K}\boldsymbol{r}_{n_1n_2n_3}$. The strength of the total scattered field of Eq. (1.7) thus sensitively depends on the spatial orientation of the wave vectors $\boldsymbol{K}_0$ and $\boldsymbol{K}$ with respect to the crystal reference frame $\{\boldsymbol{c}_i\}$.

Because a single phase shift depends on the vector product between the lattice vector and the wave vector difference $\boldsymbol{K} - \boldsymbol{K}_0$ the latter quantity is recognized as a physical quantity of its own significance and is named the scattering vector

$$\boldsymbol{Q} = \boldsymbol{K} - \boldsymbol{K}_0 \tag{1.8}$$

The scattering vector has the dimensionality of an inverse length, while its direction points along the bisection of incoming and scattered beam. The geometry is demonstrated in Fig. 1.3 and a closer inspection tells that the relation $|\boldsymbol{Q}| = 4\pi\sin\theta/\lambda$ holds for the scattering vector magnitude. This relation will be made use of extensively throughout the book and the reader should be fully aware of its derivation from Fig. 1.3. It should be realized that $|\boldsymbol{Q}|$ depends on both (a) the geometry of the scattering process via θ and (b) the wavelength λ of the probing x-ray beam. The physical meaning of $\boldsymbol{Q}$ in a mechanical analogy is that of a momentum transfer. By analogy with the kinetic theory of gases the x-ray photon

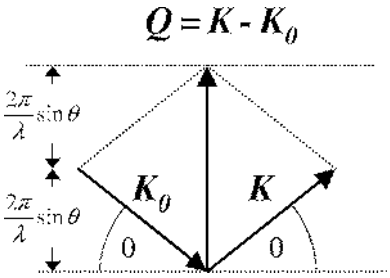


Figure 1.3 Geometry of scattering vector construction.

is compared to a gas molecule that strikes the wall and is repelled. The direction of momentum transfer follows from the difference vector between the particle's momentum before and after the event, $\boldsymbol{p} - \boldsymbol{p}_0$, while the strength of transferred momentum derives from $|\boldsymbol{p} - \boldsymbol{p}_0|$. In the case considered here the mechanical momentum $\boldsymbol{p}$ just has to be replaced by the wave vector $\boldsymbol{K}$ of the x-ray photon. This analogy explains why the scattering vector $\boldsymbol{Q}$ is also named the vector of momentum transfer. It has to be emphasized that the scattering vector $\boldsymbol{Q}$ is a physical quantity fully under the control of the experimentalist. The orientation of the incident beam ($\boldsymbol{K}_0$) and the position of the detector ($\boldsymbol{K}$) decide the direction in which the momentum transfer ($\boldsymbol{Q}$) of x-rays proceeds. And the choice of wavelength determines the amplitude of momentum transfer to which the sample is subjected. From these considerations it is possible to understand the collection of a diffraction pattern as a way of scanning the sample's structure by scattering vector variation.

If the summation factor of Eq. (1.7) is expanded into three individual terms and the geometry of the simple cubic lattice is used it is found that the field amplitude of the scattered beam is proportional to

$$\sum_{n_1=0}^{N_1-1}\sum_{n_2=0}^{N_2-1}\sum_{n_3=0}^{N_3-1}\exp\left(-i\boldsymbol{Q}\left[n_1 a\boldsymbol{c}_1 + n_2 a\boldsymbol{c}_2 + n_3 a\boldsymbol{c}_3\right]\right) \tag{1.9}$$

where the scattering vector $\boldsymbol{Q}$ has already been inserted instead of $\boldsymbol{K} - \boldsymbol{K}_0$. This expression can be converted by evaluating each of the three terms by the formula of the geometric sum. In order to arrive at the intensity the resultant product has to be multiplied by the complex conjugate and we obtain the so-called interference function

$$\Im(\boldsymbol{Q}) = \frac{\sin^2\left(N_1 a\boldsymbol{Q}\boldsymbol{c}_1/2\right)}{\sin^2\left(a\boldsymbol{Q}\boldsymbol{c}_1/2\right)}\cdot\frac{\sin^2\left(N_2 a\boldsymbol{Q}\boldsymbol{c}_2/2\right)}{\sin^2\left(a\boldsymbol{Q}\boldsymbol{c}_2/2\right)}\cdot\frac{\sin^2\left(N_3 a\boldsymbol{Q}\boldsymbol{c}_3/2\right)}{\sin^2\left(a\boldsymbol{Q}\boldsymbol{c}_3/2\right)} \tag{1.10}$$

that describes the distribution of scattered intensity in the space around the crystallite. For large values of N_1, N_2 and N_3 the three factors in $\Im(\boldsymbol{Q})$ only differ from zero if the arguments in the $\sin^2$ function of the denominator become integral multiples of π. Let us name these integers h, k and l in the following. The necessary condition to realize the highest intensity at $\boldsymbol{R}$ accordingly is

$$\Im(\boldsymbol{Q}) \to \max \Leftrightarrow \begin{aligned} a\boldsymbol{Q}\boldsymbol{c}_1 &= 2\pi h \\ a\boldsymbol{Q}\boldsymbol{c}_2 &= 2\pi k \\ a\boldsymbol{Q}\boldsymbol{c}_3 &= 2\pi l \end{aligned} \tag{1.11}$$

Here, the integers h, k, l may adopt any value between $-\infty$ and $+\infty$. The meaning of these integers compares to that of a diffraction order as known in optics from diffraction gratings. The hkl triple specifies which order one is dealing with when the primary beam coincides with zero order 000. However, the situation with a crystalline lattice is more complex, because a crystal represents a three-dimen-

sional grating and three integral numbers instead of only one indicate the order of a diffracted beam. The set of Eqs. (1.11) are the Laue conditions for the special case of cubic crystals that were derived by M. von Laue to describe the relation between lattice vectors $\boldsymbol{r}_{n_1 n_2 n_3}$ and scattering vector $\boldsymbol{Q}$ for crystals of arbitrary symmetry at the position of constructive interference.

The severe condition that is posed by Eq. (1.11) to observe any measurable intensity is illustrated in Fig. 1.4. The plot shows the course of the function $\sin^2 Nx/\sin^2 x$, for $N = 15$, which is the one-dimensional analogue of Eq. (1.10). It can be seen that the function is close to zero for almost any value of x except for $x = \pi h$, with h being an integer. At these positions the $\sin^2 Nx/\sin^2 x$ function sharply peaks and only at these points and in their vicinity can measurable intensity be observed. The sharpness of the peak rises with increasing N and a moderate value of N has been chosen to make the satellite peaks visible. It should be noted that in the case of diffraction by a crystal the three equations of Eq. (1.11) have to be obeyed simultaneously to raise $I(\boldsymbol{R})$ to measurable values. As a further property of interest it has to be mentioned that $\sin^2 Nx/x^2$ may equally be used instead of $\sin^2 Nx/\sin^2 x$ for $N \gg x$. This property will enable some analytical manipulations of the interference function, which would otherwise be possible only on a numerical basis.

In order to gain further insight into the significance of the condition for observable intensity, we will investigate the Laue conditions with respect to the magnitude of the scattering vector. The magnitude of $\boldsymbol{Q}$ at $I(\boldsymbol{R}) \rightarrow \max$ can be obtained from the three conditional Eqs. (1.11) by multiplying by the inverse cell parameter $1/a$, adding the squares and taking the square root. This yields as condition for maximum intensity

$$I(\boldsymbol{R}) \rightarrow \max \Leftrightarrow \frac{|\boldsymbol{Q}|}{2\pi} = \frac{\sqrt{h^2 + k^2 + l^2}}{a} \tag{1.12}$$

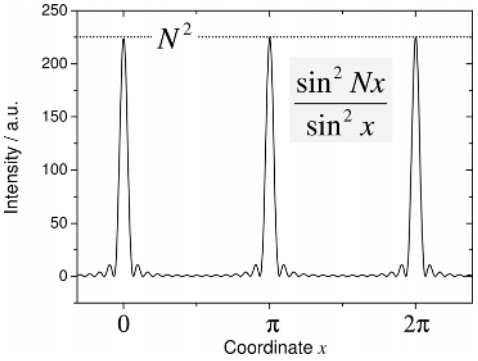


Figure 1.4 Course of the function $\sin^2 Nx/\sin^2 x$ for $N = 15$.

which can be rewritten by inserting the magnitude of the scattering vector, $|\boldsymbol{Q}| = 4\pi\sin\theta/\lambda$, known from geometrical considerations

$$I(\boldsymbol{R}) \rightarrow \max \Leftrightarrow 2\frac{a}{\sqrt{h^2+k^2+l^2}}\sin\theta = \lambda \tag{1.13}$$

This is an interesting result that may be read with a different interpretation of the *hkl* integer triple. The high degree of order and periodicity in a crystal can be envisioned by selecting sets of crystallographic lattice planes that are occupied by the atoms comprising the crystal. The planes are all parallel to each other and intersect the axes of the crystallographic unit cell. Any set of lattice planes can be indexed by an integer triple *hkl* with the meaning that a/h, a/k and a/l now specify the points of intersection of the lattice planes with the unit cell edges. This system of geometrical ordering of atoms on crystallographic planes is well known to be indicated by the so-called Miller indices *hkl*. As an example, the lattice planes with Miller indices (110) and (111) are displayed in Fig. 1.5 for the simple cubic lattice.

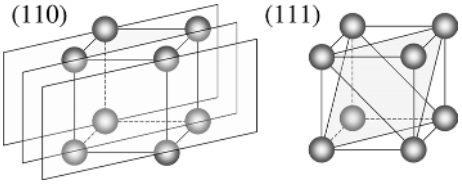


Figure 1.5 Lattice planes with Miller indices (110) and (111) in a simple cubic lattice.

The distance between two adjacent planes is given by the interplanar spacing d_{hkl} with the indices specifying the Miller indices of the appropriate lattice planes. For cubic lattices it is found by simple geometric consideration that the interplanar spacing depends on the unit cell parameter *a* and the Miller indices according to

$$d_{hkl} = \frac{a}{\sqrt{h^2+k^2+l^2}} \tag{1.15}$$

Keeping this meaning of integer triples in mind, Eq. (1.13) tells us that to observe maximum intensity in the diffraction pattern of a simple cubic crystal the equation

$$2d_{hkl}\sin\theta_B = \lambda \tag{1.15}$$

has to be obeyed. The equation is called Bragg equation and was applied by W.H. Bragg and W.L. Bragg in 1913 to describe the position of x-ray scattering peaks in angular space. The constraint $I(\boldsymbol{R}) \rightarrow \max$ has now been omitted, since it is implicitly included in using θ_B instead of θ which stands for the position of the maximum. In honor of the discoverers of this equation the peak maximum position has been named the Bragg angle θ_B and the interference peak measured in the reflection mode is termed the Bragg reflection.

The Laue conditions and the Bragg equation are equivalent in that they both describe the relation between the lattice vectors and the scattering vector for an x-ray reflection to occur. Besides deriving it from the Laue condition, the Bragg equation may be obtained geometrically, which is visualized in Fig. 1.6. A set of crystallographic lattice planes with distances d_{hkl} is irradiated by plane wave x-rays impinging on the lattice planes at an angle θ. The relative phase shift of the wave depends on the configuration of atoms as is seen for the two darker atoms in the top plane and one plane beneath. The phase shift comprises of two shares, Δ_1 and Δ_2, the sum of which equals $2d\sin\theta$ for any arbitrary angle θ. Constructive interference for the reflected wave, however, can only be achieved when the phase shift $2d\sin\theta$ is a multiple of the wavelength. Therefore, Bragg's equation is often written in the more popular form $2d\sin\theta_B = n\lambda$, where the integer n has the meaning of a reflection order. Because we are dealing with three-dimensional lattices that act as diffraction gratings, the form given in Eq. (1.14) is preferred. It should be emphasized that the Bragg equation (Eq. (1.14)) is valid for any lattice structure, not only the simple cubic one. The generalization is easily performed by just inserting the interplanar spacing d_{hkl} of the crystal lattice under investigation. Table 1.1 gives the relation of d_{hkl} and the unit cell parameters for different crystal classes.

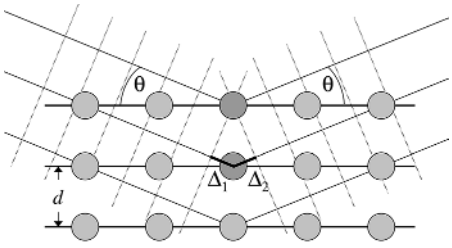


Figure 1.6 Visualization of the Bragg equation. Maximum scattered intensity is only observed when the phase shifts add to a multiple of the incident wavelength λ.

Having arrived at this point it can be stated that we have identified the positions in space where constructive interference for the scattering of x-rays at a crystal lattice may be observed. It has been shown that measurable intensities only occur for certain orientations of the vector of momentum transfer $\boldsymbol{Q}$ with respect to the crystal coordinate system $\{\boldsymbol{c}_i\}$. Various assumptions were made that were rather crude when the course of the intensity of Bragg reflections is of interest. It has been assumed, for instance, that the atom's electrons are confined to the center of mass of the atom. In addition, thermal vibrations, absorption by the specimen, etc., were neglected. More realistic models will replace these assumptions in the following. However, before doing so it should be checked how our first derivations compare with the measurement of a thin metal film and how diffraction patterns may be measured.

Table 1.1 Interplanar spacings d_{hkl} for different crystal systems and their dependency on Miller indices hkl. Parameters a, b and c give the lengths of the crystallographic unit cell, while α, β and γ specify the angles between them.

Crystal system	Constraints	$\frac{1}{d_{hkl}^2} =$
Cubic	$a = b = c$ $\alpha = \beta = \gamma = 90°$	$\frac{h^2 + k^2 + l^2}{a^2}$
Tetragonal	$a = b$ $\alpha = \beta = \gamma = 90°$	$\frac{h^2 + k^2}{a^2} + \frac{l^2}{c^2}$
Orthorhombic	$\alpha = \beta = \gamma = 90°$	$\frac{h^2}{a^2} + \frac{k^2}{b^2} + \frac{l^2}{c^2}$
Hexagonal	$a = b$ $\alpha = \beta = 90°$ $\gamma = 120°$	$\frac{4}{3}\frac{h^2 + hk + k^2}{a^2} + \frac{l^2}{c^2}$
Trigonal/ Rhombohedral	$a = b = c$ $\alpha = \beta = \gamma$	$\frac{(h^2 + k^2 + l^2)\sin^2\alpha + 2(hk + hl + kl)(\cos^2\alpha - \cos\alpha)}{a^2(1 - 3\cos^2\alpha + 2\cos^3\alpha)}$
Monoclinic	$\alpha = \gamma = 90°$	$\frac{h^2}{a^2\sin^2\beta} + \frac{k^2}{b^2} + \frac{l^2}{c^2\sin^2\beta} - \frac{2hl\cos\beta}{ac\sin^2\beta}$
Triclinic	None	Exercise 4

1.2 The $\theta/2\theta$ Scan

An often-used instrument for measuring the Bragg reflection of a thin film is the $\theta/2\theta$ diffractometer. Let us introduce its operation principle by considering the results obtained with the question in mind as to how x-ray scattering experiments are preferably facilitated. What we are interested in is the measurement of Bragg reflections, i.e. their position, shape, intensity, etc., in order to derive microstructural information from them. The intensity variation that is associated with the reflection is included in the interference function like the one given in Eq. (1.10), while the scattered intensity depends on the distance from the sample to the detection system $\boldsymbol{R}$. We therefore should configure the instrument such that we can scan the space around the sample by keeping the sample–detector distance $\boldsymbol{R}$ constant. This measure ensures that any intensity variation observed is due to the interference function and is not caused by a dependency on $\boldsymbol{R}$. The detector should accordingly move on a sphere of constant radius $\boldsymbol{R}$ with the sample in the center of it. In addition, the sphere reduces to a hemisphere above the sample, since we are only interested in the surface layer and data collection will be performed in reflection mode. The geometry is shown in Fig. 1.7.

Because the scattering of x-rays depends sensitively on the orientation of the crystal with respect to the scattering vector, we carefully have to define the various coordinate systems with which we are dealing. A sample reference frame $\{\boldsymbol{s}_i\}$ is introduced for this purpose that is oriented with $\boldsymbol{s}_1$ and $\boldsymbol{s}_2$ in the plane of the thin film, while $\boldsymbol{s}_3$ is equivalent to the surface normal.

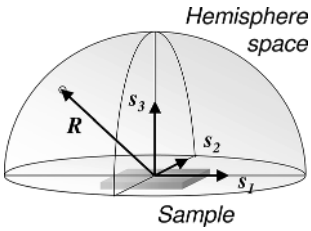


Figure 1.7 Sample reference frame $\{\boldsymbol{s}_i\}$ and hemisphere above it.

The working principle of a $\theta/2\theta$ scan is visualized in Fig. 1.8 in the hemisphere of the sample reference frame. The sample is positioned in the center of the instrument and the probing x-ray beam is directed to the sample surface at an angle θ. At the same angle the detector monitors the scattered radiation. The sample coordinate vectors $\boldsymbol{s}_1$ and $\boldsymbol{s}_3$ lie in the scattering plane defined by $\boldsymbol{K}_0$ and $\boldsymbol{K}$. During the scan the angle of the incoming and exiting beam are continuously varied, but they remain equal throughout the whole scan: $\theta_{\text{in}} = \theta_{\text{out}}$. Note that the angle convention is different from the one used in optics: in x-ray diffraction the angles of incoming and exiting beam are always specified with respect to the surface plane, while they are related to the surface normal in optics. The $\theta/2\theta$ scan can also be understood as a variation of the exit angle when this is determined with respect to the extended incoming beam and this angle is 2θ for all points in such a scan. This is the reason for naming the measurement procedure a $\theta/2\theta$ scan. The quantity measured throughout the scan is the intensity scattered into the detector. The results are typically presented as a function of $I(2\theta)$ type.

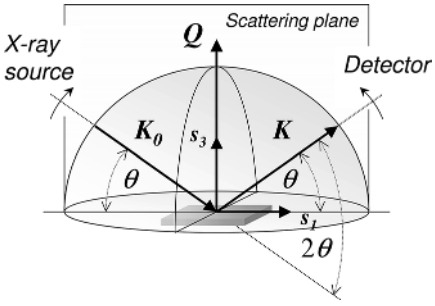


Figure 1.8 Schematic representation of a $\theta/2\theta$ scan from the viewpoint of the sample reference frame $\{\boldsymbol{s}_i\}$.

These $\theta/2\theta$ scans are extensively used for the investigation of polycrystalline samples. The measurement of polycrystals is somewhat easier than that of single crystals due to the fact that, among other reasons, the scattered intensity for constant scattering angle is distributed on a circle rather than focused to a few points in space. Interestingly, in a $\theta/2\theta$ scan the scattering vector $\boldsymbol{Q}$ is always parallel to

the substrate normal s_3. This fact is evident from Fig. 1.8 and the graphical definition of $\boldsymbol{Q}$ in Fig. 1.3. Due to this geometrical constraint only those lattice planes *hkl* that are oriented parallel to the surface plane can contribute to a Bragg reflection. The selective perception of certain subsets of crystallites in a $\theta/2\theta$ scan is visualized in Fig. 1.9. If various reflections *hkl* are measured they all stem from distinct subsets of crystallites – except they are of harmonic order, i.e. $h'k'l' = n(hkl)$.

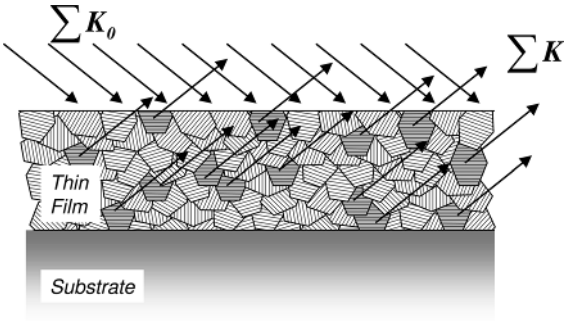


Figure 1.9 Selection principle for exclusive measurement of surface-parallel lattice planes in a $\theta/2\theta$ scan.

In order to demonstrate the principles developed so far, the simulation of a $\theta/2\theta$ scan of a 500 nm thin Al film is shown in Fig. 1.10. The simulation was calculated for the characteristic radiation of a copper x-ray tube having $\lambda(\text{Cu K}\alpha) = 0.154$ nm (see Instrumental Box 1 for further information). Various interesting features are realized from this plot, which displays eight Bragg reflections in the scattering angle range from 25° to 125°. The reflections may be assigned to their Miller indices when use is made of the Bragg equation and the unit cell parameter of the Al lattice, $a = 0.4049$ nm. For this purpose the d values of the $2\theta_B$ reflex positions have been calculated according to the Bragg equation $d = \lambda/(2\sin\theta_B)$ and checked for the solution of $(a/d)^2 = h^2 + k^2 + l^2$. It is seen that various reflections like 111 and 200 are observed, but other peaks like 100, 110, etc., are missing. This phenomenon has to be understood in the sense of destructive interference, which is caused by the structure of the Al lattice, which is distinct from the simple cubic lattice. It has to be noted that a splitting of peaks into an α_1 peak and an α_2 peak cannot be observed, although the feature was included in the simulation. The absence is explained from the broadness of the Bragg peaks causing a severe overlap between both peaks such that they remain unresolved. Broad reflections are caused by small grain sizes and crystal lattice faults that are often observed in thin polycrystalline films and are discussed in more detail in Chapter 3. Moreover, the diffraction pattern exhibits a pronounced decrease of scattered intensity with increasing scattering angle. Therefore, the diffraction pattern is also shown in the inset with a $\sqrt{I}$ ordinate in order to emphasize the smaller peaks. The square-root intensity plot is an often-used presentation mode. It is concluded that the basic features of Section 1.1

are in accordance with the simulated measurement of a thin Al film, but some aspects remain to be clarified.

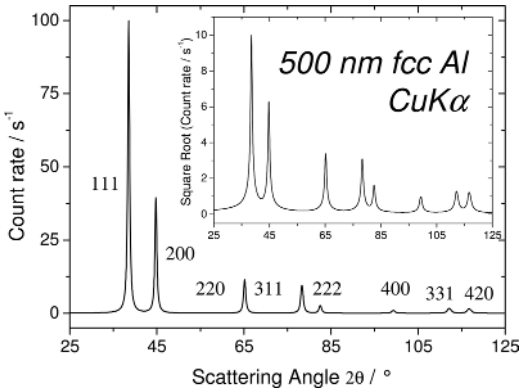


Figure 1.10 Simulation of a $\theta/2\theta$ scan of a 500 nm thin Al film measured with Cu Kα radiation. The inset shows the same pattern with a $\sqrt{\text{I}}$ ordinate.

1.3 Intensity of Bragg Reflections

The necessary refinement of the expression for the intensity of a Bragg reflection is now developed. For this purpose the finding will be used that was made by deriving the Bragg equation and the Laue conditions. It has been realized that the amplitude of the total scattered field from a charge distribution in the Fraunhofer approximation is characterized by a phase factor $\exp(-\text{i}\boldsymbol{Q}\boldsymbol{r}_{n_1n_2n_3})$ comprising the scattering vector $\boldsymbol{Q}$ and the distance $\boldsymbol{r}_{n_1n_2n_3}$ between all pairs of point charges. This result may be generalized by subjecting the sum in Eq. (1.9) to a continuous limit. Instead of writing a discrete distance vector $\boldsymbol{r}_{n_1n_2n_3}$ the continuous variable $\boldsymbol{r}$ is used and it is argued that the scattered field depends as

$$\int \rho_{\text{e}}(\boldsymbol{r}) \exp(-i\boldsymbol{Q}\boldsymbol{r}) d\boldsymbol{r} \tag{1.16}$$

on the electronic charge distribution $\rho_{\text{e}}(\boldsymbol{r})$ of the scattering object. The integration has to be performed over the volume $d\boldsymbol{r}$ to which the scattering electrons are confined. Because ρ_{e} has the dimensionality of an inverse volume the integration yields a dimensionless quantity, which is in accordance with our starting point. This new expression can now be applied to the scattering objects in which we are interested, i.e. atoms and crystallographic unit cells, to check whether the provisional intensity function is improved.

Instrumental Box 1:

$\theta/2\theta$ Diffractometer

The basic measurement geometry of by far the most frequently used x-ray diffraction instrument is depicted in Fig. i1.1. The sample should preferably exhibit a plane or flattened surface. The angle of both the incoming and the exiting beam is θ with respect to the specimen surface. A vast number of organic and inorganic powder samples have been measured with these instruments from which the naming of powder diffractometer is understood. Its measurement geometry may also be applied to the investigation of thin films, especially if the layer is polycrystalline and has been deposited on a flat substrate, as is often the case.

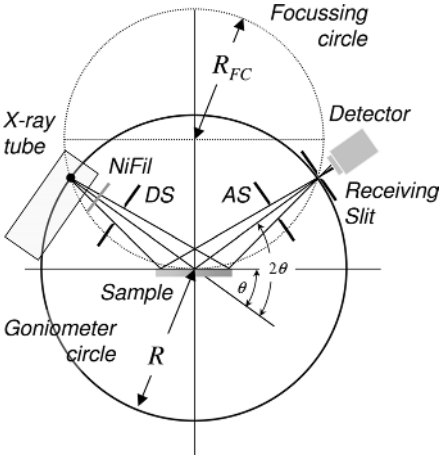


Figure i1.1 Schematic representation of $\theta/2\theta$ diffraction in Bragg–Brentano geometry.

The diffraction pattern is collected by varying the incidence angle of the incoming x-ray beam by θ and the scattering angle by 2θ while measuring the scattered intensity $I(2\theta)$ as a function of the latter. Two angles have thus to be varied during a $\theta/2\theta$ scan and various types of powder diffractometers are in use. For one set of instruments the x-ray source remains fixed while the sample is rotated around θ and the detector moves by 2θ. For other systems the sample is fixed while both the x-ray source and the detector rotate by θ simultaneously, but clockwise and anticlockwise, respectively. The rotations are performed by a so-called goniometer, which is the central part of a diffractometer. A goniometer of a powder diffractometer comprises at least two circles or – equally – two axes of rotation. Typically the sample is mounted on the rotational axis, while the detector and/or x-ray source move along the periphery, but both axes of rotation coincide. In most laboratory $\theta/2\theta$ diffractometers the goniometer radius, which is the sample-to-detector distance, is in the range 150–450 mm. Highly precise goniometers with 0.001°

precision and even lower on both the θ and the 2θ circles are commercially available. The collected diffraction pattern $I(2\theta)$ consists of two sets of data: a vector of $2\theta_i$ positions and a second vector with the appropriate intensities I_i. The step size $\Delta 2\theta_i$ between two adjacent $2\theta_i$ should be chosen in accordance with the intended purpose of the data. For chemical phase analysis (Chapter 2) the full width of half the maximum of the tallest Bragg peak in the pattern should be covered by at least 5 to 7 measurement points. However, for a microstructural analysis (Chapter 3) in excess of 10 points should be measured on the same scale. The appropriate value of $\Delta 2\theta_i$ will also depend on the slit configuration of the diffractometer. The preset integration time of the detector per step in $2\theta_i$ should allow the integral intensity of the smallest peak of interest to exceed the noise fluctuations $\sigma(I)$ by a factor of 3 or 5, etc., according to the required level of statistical significance.

The control of the x-rays beam bundle suffers from the constraint that lenses and other refractive elements are not as easily available as those used for visible light. For this reason the beam conditioning in $\theta/2\theta$ diffractometers is mostly performed by slits and apertures and may be termed shadow-casting optics. In addition, powder diffractometers have to deal with the divergent beam characteristic that is emitted by an x-ray tube. Most systems operate in the so-called Bragg–Brentano or parafocusing mode. In this configuration a focusing circle is defined as positioned tangentially to the sample surface (see Fig. i1.1). The focusing condition in the Bragg–Brentano geometry is obeyed when the x-ray source and detector are positioned on the goniometer circle where it intersects the focusing circle. True focusing would indeed occur only for a sample that is bent to the radius of the focusing circle R_{FC}. Since R_{FC} differs for various scattering angles 2θ, true focusing cannot be obtained in a $\theta/2\theta$ scan and the arrangement is thus termed parafocusing geometry.

In a $\theta/2\theta$ scan the scattering vector $\boldsymbol{Q}$ is always parallel to the substrate normal. It is, however, evident from the above considerations and from Fig. i1.1 that this is strictly valid only for the central beam, while slight deviations from the parallel orientation occur for the divergent parts of the beam. If the most divergent rays deviate by $\pm\delta$ from the central beam their scattering vector is tilted by δ from the sample normal – at least for those scattering events that are received by the detector. In many configurations of diffractometer optics it suffices to consider only the central beam.

The analysis and interpretation of x-ray diffraction measurements necessitates distinguishing three different reference frames that are assigned to the laboratory, the sample and the crystallites and symbolized by $\{\boldsymbol{l}_i\}$, $\{\boldsymbol{s}_i\}$ and $\{\boldsymbol{c}_i\}$, respectively. The unit vectors in each system are denoted by $\boldsymbol{l}_i$, $\boldsymbol{s}_i$ or $\boldsymbol{c}_i$, with i ranging from 1 to 3 for the three orthogonal directions. Transformations between these coordinate systems are frequently used, for which unitary transformation matrices a_{ij} are defined with superscripts LS, SC, CL, etc., indicating the initial and the final reference frame. The relations are visualized in Fig. i1.2.

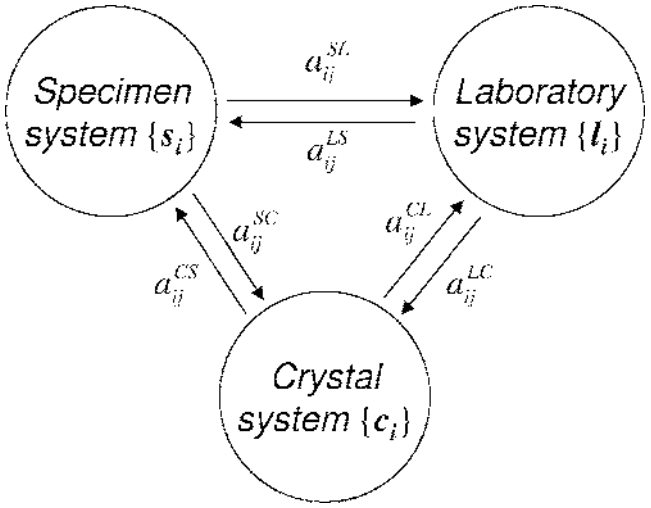


Figure i1.2 The three reference frames used in x-ray diffraction and the appropriate transformation matrices between them.

1.3.1 Atomic Form Factors

Formula (1.16) can be applied to atoms by inserting the square of electronic wavefunctions for the charge density $\rho_e(\boldsymbol{r})$. Before the results of this procedure are presented let us first investigate what might be expected from basic physical considerations. For this purpose the electrons may temporarily be imagined in the atomic model of Bohr to move in circular orbits around the nuclei. If the scattering from any two arbitrary electrons from this atom could be obtained it is evident that the scattering may occur for many different distance vectors $\boldsymbol{r}$ being associated with a large variation of phase shifts $-i\boldsymbol{Qr}$. The orbital smearing of the electron density will thus lead to a cessation of coherency and a reduction in the coherently scattered intensity. This reduction will be stronger the larger $\boldsymbol{Q}$ becomes, because it is the scalar product $\boldsymbol{Qr}$ that determines the phase shift.

The ansatz is made that the scattering of an atom depends on the shape of the electron density function or on its form, and we thus define an atomic form factor f by

$$f = \int_{at} \rho_e(\boldsymbol{r}) \exp(-i\boldsymbol{Qr}) d\boldsymbol{r} \tag{1.17}$$

In the limit of $\boldsymbol{Q} = 0$ the integration just runs over the charge distribution and yields the number of electrons of the atom Z. For $\boldsymbol{Q} \neq 0$ the form factors are rea-

sonably presented as a function of $|\boldsymbol{Q}|$ or $\sin\theta/\lambda$. Atomic form factors have been calculated with various quantum mechanical methods of increasing sophistication. A compilation of values for all chemical elements and some important ions is given in Ref. [1]. Moreover, very often an approximation of f in the form of the model function

$$f = \sum_{j=1}^{4} a_j \exp\left(-b_j \sin^2\theta / \lambda^2\right) + c_j \tag{1.18}$$

is used. By this approach a precision of 10^{-6} is achieved for the form factors and only nine coefficients have to be given for any atom or ion to model the whole $\sin\theta/\lambda$ range. The coefficients a_j, b_j and c_j are also tabulated in Ref. [1].

It is concluded that point charges Ze have to be substituted by fe in all the foregoing expressions in order to deal correctly with the extension of atomic charge distributions. For some metallic atoms the atomic form factors as calculated by Eq. (1.18) are displayed in Fig. 1.11. For low scattering angles they can be seen to reach values close to the atomic number Z, but a steep decrease with increasing $\sin\theta/\lambda$ is clearly seen for all of them. It should be noted that the intensity scales with the square of the atomic form factor and that an even stronger decrease will occur for f^2. For the example of Nb the form factor for the fivefold ion Nb^{5+} is also given. It can be seen that a difference between atoms and their ions is only significant for f values at low $\sin\theta/\lambda$, which is a general tendency for all atoms and ions, not just for Nb.

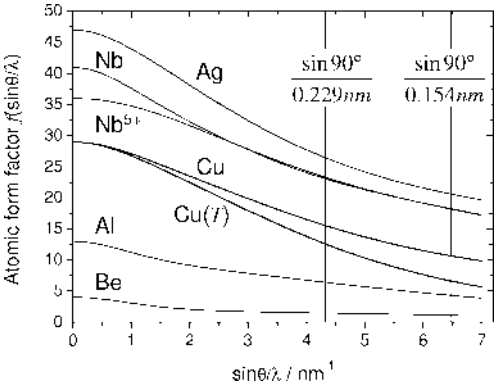


Figure 1.11 Atomic form factors of Be, Al, Cu, Cu@fccCuRT, Nb, Nb^{5+} and Ag.

For some investigations the inelastic scattering of x-rays cannot be neglected and the concept of the atomic form factors will then have to be extended by including real and imaginary anomalous scattering factors, f' and f'', that have to be added to the atomic form factors f given above. In most cases, anomalous scattering factors f' and f'' are small when compared with f. Numerical values for f' and f'' are given in the Ref. [1].

1.3.2 Structure Factor

The crystallographic unit cell is the smallest unit by which the periodic order in the crystal is repeated. In the simple cubic lattice that has been considered to derive the Bragg and Laue equations there is only one atom per unit cell. The scattered intensity was found to scale with the square of the charge of this atom – or the form factor as should be said now – and the interference function, see Eq. (1.10). For more complex structures the integration has to be extended over the total charge distribution of the unit cell (uc) rather than over a single atom. This quantity is denoted as the structure factor $\boldsymbol{F}$ that is given by

$$\boldsymbol{F} = \int_{\mathrm{uc}} \rho_{\mathrm{e}}(\boldsymbol{r}) \exp(-i\boldsymbol{Q}\boldsymbol{r}) d\boldsymbol{r} \tag{1.19}$$

We will symbolize it consistently by a bold letter, since it is a complex quantity. The expression for the structure factor may be simplified by recalling that the unit cell comprises N atoms, numbered by n from 1 to N. It is thus possible to decompose the structure factor into single shares due to the individual atoms (at)

$$\boldsymbol{F} = \sum_{n=1}^{N} \int_{\mathrm{at}} \rho_{\mathrm{e}}(\boldsymbol{r}) \exp\left(-i\boldsymbol{Q}(\boldsymbol{r} - \boldsymbol{r}_n)\right) d\boldsymbol{r} \tag{1.20}$$

and the integration just has to be performed over the charge distributions of individual atoms. These values are known: they are given by the atomic form factors f_i of the nth atom. Accordingly, the structure factor can be written

$$\boldsymbol{F} = \sum_{n=1}^{N} f_n \exp\left(i\boldsymbol{Q}\boldsymbol{r}_n\right) \tag{1.21}$$

The product of the scattering factor with the positions $\boldsymbol{r}_n$ of the N various atoms in the unit cell thus has to be evaluated. The latter are specified by their fractional coordinates (x_n, y_n, z_n) that read for the cubic cell $\boldsymbol{r}_n = x_n a\mathrm{c}_1 + y_n a\boldsymbol{c}_2 + z_n a\boldsymbol{c}_3$. We know that reflection intensity may only be observed when the Laue conditions are simultaneously obeyed which may be applied to simplify the phase factor by

$$\boldsymbol{Q}(x_n a\boldsymbol{c}_1 + y_n a\boldsymbol{c}_2 + z_n a\boldsymbol{c}_3) = hx + ky + lz \tag{1.22}$$

Only if this equation is obeyed does measurable intensity from interfering x-rays enter into the detector and the scattering of the crystal scales with

$$\boldsymbol{F}(hkl) = \sum_{n=1}^{N} f_n \exp\left[2\pi i(hx_n + ky_n + lz_n)\right] \tag{1.23}$$

The structure factor thus depends on the Miller indices of the reflection under consideration, the positions of the atoms in the unit cell and the atomic scattering factor. In monoatomic lattices the form factor is the same for all atoms and can be placed in front of the sum. For the simple cubic structure $N = 1$ and $x = y = z = 0$ and thus $\boldsymbol{F} = f$ for all hkl and reflections are observed for each order; however, for

more complicated structures the full structure factor has to be investigated. Although the derivative has only been given for the cubic lattice it has to be emphasized that the expression for the structure factor, Eq. (1.23), is valid for crystals of arbitrary symmetry.

The majority of one-elemental metals are found in either the face-centered cubic (fcc), the body-centered cubic (bcc) or the hexagonal close-packed (hcp) structure. The relative arrangement of atoms in theses lattices is presented in Structure Box 1. Aluminum, for instance, crystallizes in the fcc structure. In this case the Bragg equation might be obeyed for certain lattice planes *hkl*, but for some combinations of *hkl* the phase shift in the x-rays scattered by neighboring atoms may amount to π or odd multiples of it. The scattered beams then interfere destructively and the reflections for these lattice planes are not extincted. In the fcc structure, for instance, destructive interference occurs for *hkl* = 100, 110, etc.

The extinction conditions can be derived for any crystal lattice by performing the same summation procedure that has been performed for the simple cubic lattice in the first section and it is an instructive exercise to do so (Exercise 7). One will then arrive at conditions comparable to Eq. (1.11) which predict under which orientation of $\boldsymbol{Q}$ towards $\{\boldsymbol{s_i}\}$ reflections might be observed. A simpler approach instead is the calculation of the structure factor. Inserting the fractional coordinates of all four atoms of the fcc structure in Eq. (1.23) yields the result

$$\boldsymbol{F}_{\mathrm{fcc}}(hkl) = f\begin{bmatrix}1+\exp(i\pi(h+k))+\\ \exp(i\pi(h+l))+\exp(i\pi(k+l))\end{bmatrix} = \begin{cases}4f & \text{all } hkl \text{ even/odd}\\ 0 & hkl \text{ mixed}\end{cases} \tag{1.24}$$

The expression is seen to vanish for certain *hkl* and the lower equation is thus denoted as an extinction condition. It means that Bragg reflections are only observed for the fcc lattice if all Miller indices are either even or odd. For mixed triples destructive inference occurs and these reflections are systematically absent. It is evident from the $\theta/2\theta$ scan in Fig. 1.10 that this pattern in fact is in accordance with the extinction conditions of the fcc structure. Mathematically speaking, the Bragg equation is a necessary but not a sufficient condition for x-ray reflections to arise.

The structure factor of the bcc lattice can be obtained in the same way and results in

$$\boldsymbol{F}_{\mathrm{bcc}}(hkl) = f\left[1+\exp(i\pi(h+k+l))\right] = \begin{cases}2f & h+k+l=2n\\ 0 & \text{otherwise}\end{cases} \tag{1.25}$$

The extinction condition now derives from a sum over Miller indices and reads that the sum must yield an even number for the reflection to occur. Only if this condition is obeyed is the interference nondestructive and can be detected at the position predicted by Bragg's equation (Eq. (1.15)). The structure factor for the hcp structure can be derived as an exercise from the atom coordinates in the unit cell.

The structure factor $\boldsymbol{F_h}$ from a reflection $\boldsymbol{h}$ is of central importance in x-ray diffraction, because it relates the position of the atoms in the unit cell to the intensity of a reflection. Here, the Miller index triple *hkl* has been abbreviated by the subscript $\boldsymbol{h}$ which will be used very often in the following. The intensity scales with the product of $\boldsymbol{F}$ and its complex conjugate $\boldsymbol{F}^*$. As can be seen from the examples of the

Structure Box 1:

Elementary Metals

The simple cubic structure that is used in this chapter to derive the basic formulas of x-ray diffraction only rarely occurs in nature. It is instead observed that one-elemental crystal lattices often take the face-centered cubic (fcc) or the body-centered cubic (bcc) structure. Figure s1.1 displays both of them. The interatomic distances are fully specified by the unit cell edge a. Each atom is surrounded by eight neighbor atoms in the bcc structure or twelve in the fcc structure. Besides the cubic structures, various metals are found to crystallize in the hexagonal close-packed (hcp) structure, also shown in Fig. s1.1. This structure has two degrees of freedom, namely the interatomic distance a in the base plane and the distance between two of the planes, $c/2$. Accordingly, two distinct interatomic distances r_1 and r_2 occur between next neighbors in the hcp structure (Exercise 1.12). An inspection of the periodic system reveals that the majority of elements assume one of these three basic structures under thermodynamic standard conditions (298 K, 101.6 kPa).

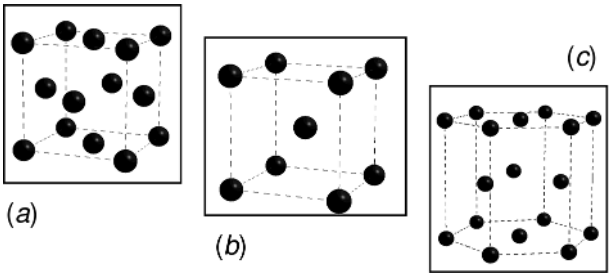


Figure s1.1 Crystallographic unit cells of the most frequently occurring structures of one-elemental metals: (a) face-centered cubic, (b) body-centered cubic and (c) hexagonal close-packed structure.

In both the fcc and hcp structures the atoms are arranged according to the model of close-packed spheres. It is thereby assumed that the atoms can be modeled by rigid spheres that all exhibit the same radius r_{at}. The value of r_{at} is chosen such that atomic neighbors are in contact via their surfaces. According to this scheme the atomic radius can be calculated and is found to be $r_{at,fcc} = a\sqrt{2}\,/\,4$ in the fcc structure. In the hcp structure the condition can only be obeyed when $r_1 = r_2$ holds, which leads to $r_{at,hcp} = a$ or equivalently $c/a = \sqrt{8/3} = 1.633$. The c/a parameter in general serves to define the ideal hcp structure, which is a close-packed one. In one-elemental metals with the hexagonal Mg structure the c/a ratio is always found to be very close to this ideal value (see Table s1.1). Although these structures deviate slightly from the ideal hcp structure, they are often considered hcp structured anyway and the value of c/a is specified additionally. If the volume of atomic spheres in both the fcc and the hcp structure is calculated and normalized with respect to the unit cell volume V_{uc}, a value of 0.74 results for the volume

Table s1.1 The three most common crystal structures of one-elemental metals. Unit cell edges under standard conditions are given.

Structure	Strukturbericht designation	Space group	Atomic positions		Examples with lattice parameters *a* and *c* (nm)
Face-centered cubic (fcc)	Copper structure (A1)	$Fm\bar{3}m$ (225)	000 ½0½	0½½ ½½0	Al: 0.4049; Ni: 0.3524 Cu: 0.3615; Ag: 0.4086
Body-centered cubic (bcc)	Tungsten structure (A2)	$Im\bar{3}m$ (229)	000	½½½	Cr: 0.2884; Fe: 0.2866 Nb: 0.3307; W: 0.3165
Hexagonal close-packed (hcp)	Magnesium structure (A3)	$P6_3/mmc$ (194)	000	⅔⅓½	Mg: 0.3209, 0.5210 Ti: 0.2950, 0.4879 Zn: 0.2665, 0.4947 Zr: 0.3231, 0.5147

ratio. This is the largest value of spatial filling that might be achieved by the packing of spheres all having the same diameter.

It should be noted that crystallographic lattice planes in the hcp and also in other hexagonal structures are indexed by four Miller indices (*hkil*), where always $i = -(h + k)$ holds. This indexing results from the usage of three unit vectors in the basal plane of hexagonal unit cells. In a widely used abbreviation a period is simply inserted for the third index: (*hk.l*). One immediately realizes from the occurrence of both types of Miller index symbol that a hexagonal structure is being considered.

There exists an interesting relation between the close-packed fcc and hcp structures. The relation becomes evident when all atoms in the fcc lattice are decomposed into atomic (111) planes and compared with the (00.1) planes in the hcp structure (see Fig. s1.2). The coordination within the plane is the same, i.e. each sphere is surrounded by six neighbors to yield the highest packaging density of spheres within the plane. Looking from above on the plane stacking reveals that there exist three distinct positions where atoms might become situated, which are named A, B and C. In each plane atoms are positioned at A, B or C. It turns out that the stacking of planes may be accounted for by the sequences ...ABCABC... in the fcc structure, but by ...ABABAB... in the hcp structure. Therefore, both structures just differ by the vertical stacking sequence of fully occupied atom planes.

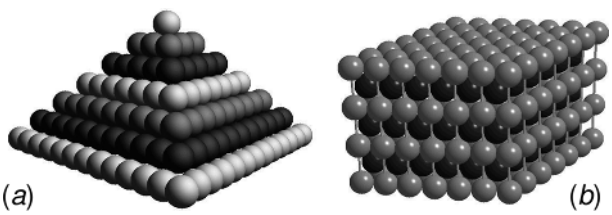


Figure s1.2 Stacking of close-packed planes in (a) fcc and (b) hcp structures.

fcc and bcc lattice the magnitude of $\boldsymbol{F}$ maximally equals the number of atoms in the unit cell multiplied by their atomic form factor. This situation is rarely observed for more complicated structures, because the scattering of the different groups of atoms often causes a partial destructive interference. This fact is demonstrated from the structure factors of technologically relevant compounds that are found in the various structure boxes of subsequent chapters.

The structure factor has the mathematical form of a discrete Fourier transform. The reverse transformation from the intensity of observed reflections would thus allow the determination of the atomic positions in the unit cell. However, the intensity scales with the product of the structure factor and its complex conjugate, $\boldsymbol{F_h F_h^*}$, which is associated with a severe loss of information. If the structure factor is plotted in the Euler plane of complex numbers it may be characterized by its magnitude $|\boldsymbol{F_h}|$ and its phase $\phi_{\boldsymbol{h}}$. In this picture the information loss can be envisaged as a loss of phase information, which is the well-known phase problem in the structure determination by x-ray diffraction.

Regarding the effect of thermal vibrations the same arguments apply as given above to justify the reduction in coherency by the spatial extension of electronic charge distribution. It is well known that the atoms in a solid oscillate at their equilibrium positions $\boldsymbol{r_n}$. Temperature vibrations entail a reduction of phase coherence in the scattered beam and thus reduce the measured intensity. The phenomenon can quantitatively be accounted for by the mean quadratic deviation $\overline{u^2}$ of the atom from its average position r_n. The atomic form factors f have then to be replaced by the temperature-dependent expression

$$f_T = f \exp\left(-8\pi\overline{u^2}\sin^2\theta / \lambda^2\right) \tag{1.26}$$

Again, it can be seen that the scattering amplitude is exponentially damped with increasing scattering angle and that the damping coefficient scales with the square of momentum transfer $4\pi\sin\theta/\lambda$. The $8\pi\overline{u^2}$ factor is often abbreviated by the symbol B in the literature. Typically the average displacements of atoms $\sqrt{\overline{u^2}}$ at room temperature are in the range between 0.005 and 0.03 nm, which translates into a few percent to more than 10% of the bond length. In the fcc structured Cu lattice, for instance, $\sqrt{\overline{u^2}}$ amounts to about 6% of $d_{\text{Cu-Cu}}$. The effect of the temperature vibrations can be seen from Fig. 1.11, where in addition to the zero-temperature f also the atomic form factor of Cu in the Cu lattice is shown. It is evident that the scattering strength may be significantly reduced by thermal vibration, which holds in particular for high scattering angles.

These results are applied to the structure factor simply by replacing the form factor with its temperature-dependent value

$$\boldsymbol{F}_{hkl}(T) = \sum_{n=1}^{N} f_n \exp\left(-B_n(T)\sin^2\theta / \lambda^2\right)\exp\left(2\pi i(hx_n + ky_n + lz_n)\right) \tag{1.27}$$

Because the thermal vibration amplitudes increase with increasing temperature the damping of Bragg reflections will also increase. This causes the Bragg reflection to sink into a background of diffuse scattered intensity when the temperature

is increased. This is in contrast to many spectroscopic techniques, where the observed peaks broaden at elevated temperature.

1.3.3 Multiplicity

The multiplicity specifies the number of equivalent lattice planes that may all cause reflections at the same θ_B position. The phenomenon is visualized in Fig. 1.12, for the laboratory in reference frame $\{\boldsymbol{l}_i\}$. In this coordinate system the position of the incoming beam is set constant with its direction pointing along the $\{\boldsymbol{l}_i\}$ system unit vector $\boldsymbol{l}_1$. While $\boldsymbol{K}_0$ is fixed, $\boldsymbol{K}$ moves on a circle during a $\theta/2\theta$ scan as does the substrate normal $\boldsymbol{s}_3$. The figure displays the position during the scan when θ is at the Bragg angle of Al (111). In the case where the sample comprises a single Al crystal of (111) orientation three further reflections would equally be excited at the intersection of the $2\theta_{111}$ cone with the $\{\boldsymbol{l}_i\}$ sphere. The reflections would be caused by the equally probable scattering of the incoming x-ray beam at lattice planes $(\bar{1}11)$, $(1\bar{1}1)$ and $(11\bar{1})$ that all exhibit the same interplanar spacing d_{111} to obey the Bragg equation. In the case of a polycrystalline sample being measured, however, the intensity would look totally different. Because of the random orientation of crystallites the intensity of all equivalent (111) planes would be equally distributed on a cone of opening angle 4θ rather than being concentrated in a few singular spots. The intensity would be smeared out over a ring shown as a grey line in Fig. 1.12. There are $m_{111} = 8$ equivalent (111) planes, but only $m_{200} = 6$ for (200) and it is evident that the multiplicity $m_{\boldsymbol{h}}$ will enter the expression of a Bragg reflection intensity as a scaling factor.

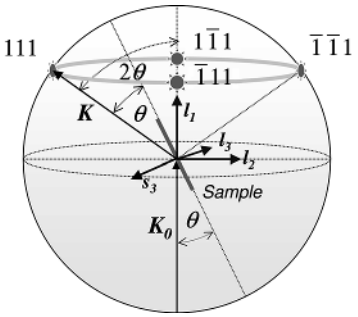


Figure 1.12 Scattering in the laboratory reference frame $\{\boldsymbol{l}_i\}$ for a 111 reflection from an Al single crystal of [111] orientation and a polycrystalline Al powder sample.

1.3.4
Geometry Factor

The spreading of the Bragg peak over a circular segment of the $\{\boldsymbol{l}_i\}$ sphere as discussed above introduces a further θ dependency into the diffraction pattern of a $\theta/2\theta$ scan. The effect is visualized in Fig. 1.13 where the set of all diffracted intensity for scattering angle 2θ is symbolized by a cone of opening angle 4θ. The circumferences of the intensity rings scale with $\sin 2\theta$ causing a dilution of intensity by $1/\sin 2\theta$. There also arise a variety of scattering vectors $\boldsymbol{Q}$ that lie on a cone. The scattered intensity will scale with their density, which is $\sin(\pi/2 - \theta) = \cos\theta$. The geometry factor is the product of both density functions and it is finally obtained as $G = \cos\theta/\sin 2\theta = 1/(2\sin\theta)$.

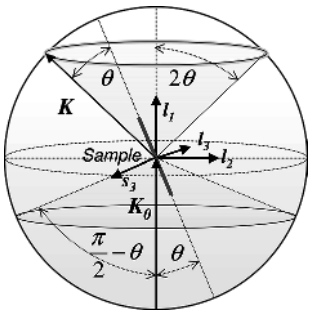


Figure 1.13 Scattering in the laboratory reference frame $\{\boldsymbol{l}_i\}$ to derive the geometry factor G.

1.3.5
Preferred Orientation (Texture)

For a powder sample it may generally be assumed that all grain orientations occur with the same probability, i.e. that the distribution function of grain orientations is isotropic. It is a characteristic structural feature of thin polycrystalline films that certain crystallographic lattice planes can occur with a greater probability than others. This phenomenon is termed preferred orientation or texture. It is evident from Fig. 1.12 that a texture might have a significant influence on the diffraction pattern, where density-enhanced lattice planes will be associated with an increase of the corresponding Bragg reflection intensity $I_{\boldsymbol{h}}$. The intensity then has to be scaled with the density of crystallite orientations that are indicated by the texture factors $T_{\boldsymbol{h}}$. For a random orientation $T_{\boldsymbol{h}} = 1$ holds for all of them. The measurement of texture and the determination of orientation distribution functions are outlined in detail in Chapter 5.

1.3.6
Polarization Factor

The x-ray radiation emitted from a laboratory x-ray tube is of random polarization. Therefore, the scattering by a polycrystalline sample has to be decomposed into a σ component and a π component. These considerations have already been outlined for the scattering by a single electron and they equally apply to the case considered here. In the case that $I_\sigma = I_\pi = I_0/2$ is valid on the average, the polarization factor takes the form

$$\overline{C^2} = \frac{1+\cos^2 2\theta}{2} \tag{1.28}$$

and it is by this factor that the intensity received by the detector has to be scaled.

The geometry factor may be different for measurement configurations other than the $\theta/2\theta$ scan. The experimentalist should check this point carefully if integral intensities have to be analyzed quantitatively. The dependency of the geometry factor G and the polarization factor $\overline{C^2}$ are both shown in Fig. 1.14 as a function of scattering angle 2θ. Also the Lorentz factor L is shown that will be derived later and the product $G\overline{C^2}L$ of all three factors. The product function is seen to exhibit a pronounced minimum close to $2\theta = 120°$. Up to this point $G\overline{C^2}L$ continuously decreases, but recovers for high scattering angles close to $2\theta_{max} = 180°$.

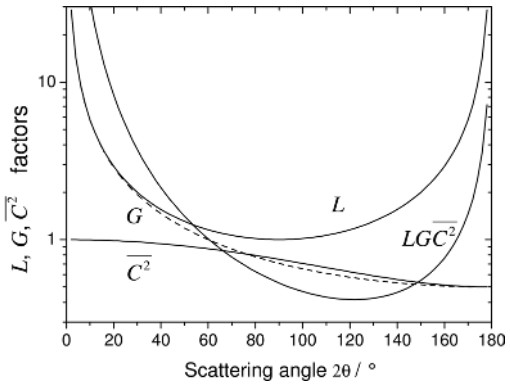


Figure 1.14 Geometry factor G, polarization factor $\overline{C^2}$ and Lorentz factor L as a function of 2θ. Also the product of the three factors is shown. Note the logarithmic ordinate scale.

1.3.7
Absorption Factor

During their transit through matter x-rays suffer from an attenuation of intensity caused by their absorption. The Lambert–Beer law, well known from optics, can describe the absorption effect. The intensity I_0 that enters into the sample will be exponentially damped to an amount $I_0\exp(-2\mu\ell)$ after a path of 2ℓ. The parameter μ

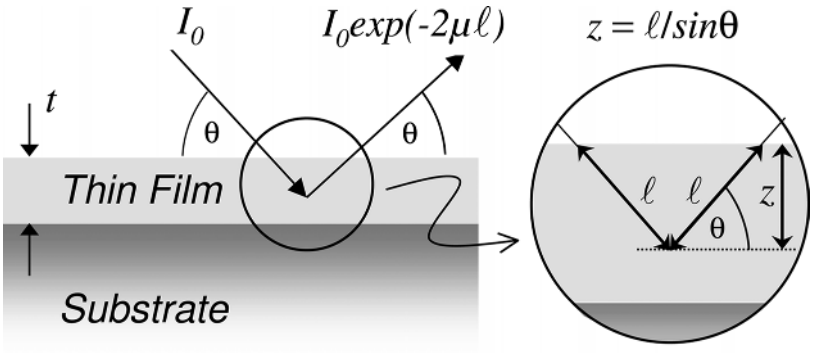


Figure 1.15 Schematic representation of the absorption effect for a thin-film sample in a $\theta/2\theta$ scan.

is named the linear attenuation coefficient and depends on the wavelength of the radiation used, the chemical composition of the sample and its density. The inverse of μ would give a penetration depth for normal incidence $\tau_{1/e} = 1/\mu$ that specifies the path length for which the intensity I_0 drops to $1/e$ of its initial value. The dimensions of the attenuation coefficient are m^{-1} or μm^{-1}. Often, the value of the mass absorption coefficient μ_m is listed in various tables that can be converted into $\mu = \rho\ \mu_m$ by multiplication with the mass density ρ. For many substances attenuation coefficients of the order of 10^5 to 10^7 m^{-1} are obtained for Cu Kα or comparable wavelengths. This corresponds to penetration depths $\tau_{1/e}$ of 0.1 to 10 µm and thus is in the range of a typical layer thickness. It can be concluded that absorption effects might significantly affect Bragg reflections of thin films.

The dominant effect the absorption factor has on a diffraction pattern is the variation of the scattered intensity. Its derivation is shown in Fig. 1.15 for the case of a $\theta/2\theta$ scan. For any x-ray beam that has traveled through a sample to become scattered into the detector the primary intensity has been reduced by the factor $\exp(-2\mu\ell)$. The reduction of intensity of the total x-ray beam is the sum over all possible paths of the beam within the limits of 0 to ℓ_{max}

$$\int_0^{\ell_{max}} \exp(-2\mu\ell)d\ell \tag{1.29}$$

The path 2ℓ that is traversed by the x-ray beam may be expressed by the depth variable z for which $\ell = z/\sin\theta$ holds. Then ℓ is substituted by $z/\sin\theta$, $d\ell$ by $dz/\sin\theta$ and the integration is performed from 0 up to the thickness t of the film. Here, $z = 0$ accounts for the surface of the film and $z = t$ for the film–substrate interface. The solution of the integral yields

$$\frac{1}{2\mu}\left\{1 - \exp\left(-\frac{2\mu t}{\sin\theta}\right)\right\} \tag{1.30}$$

In the limit of an infinitely thick sample, $t \to \infty$ which is equivalent to $t \gg 1/\mu$, the result $1/(2\mu)$ is obtained. In the following the absorption factor is denoted by

the ratio of the absorption for a sample of finite thickness with respect to an infinitely thick sample

$$A = \int_0^t \Big/ \int_0^\infty \tag{1.31}$$

The application of this procedure results in the absorption factor for the $\theta/2\theta$ configuration

$$A_{\theta 2\theta} = \left(1 - \exp\left(-\frac{2\mu t}{\sin\theta}\right)\right) \tag{1.32}$$

The subscript $\theta/2\theta$ has been added in order to indicate the measurement geometry. We will become acquainted with various A factors in the following chapters for different diffractometer configurations. The A factor is also termed the thickness factor and it is seen to cause the measured intensity to cease as a function of increasing scattering angle 2θ. In Fig. 1.16 the $A_{\theta 2\theta}$ factor is displayed for thin Al and Nb films of 500 nm and 1 μm thickness measured with Cu Kα radiation, where use has been made of the material parameters

$$\text{Al: } \mu_m = 486.7 \text{ m}^2 \text{ kg}^{-1},\ \rho = 2700 \text{ kg m}^{-3} \Rightarrow \mu = 1.31 \times 10^6 \text{ m}^{-1}$$

$$\text{Nb: } \mu_m = 1492 \text{ m}^2 \text{ kg}^{-1},\ \rho = 8550 \text{ kg m}^{-3} \Rightarrow \mu = 1.276 \times 10^7 \text{ m}^{-1}$$

The general decrease of $A_{\theta 2\theta}$ can easy be understood from the fact that the x-ray beam enters the sample under increasingly steeper angles and accordingly "sees" less sample volume for increasing 2θ. It is seen from the plot that $A_{\theta 2\theta}$ approaches unity the thicker the film or the larger is μ. Accordingly, the absorption factor depends on the product of both, which is called the μt product in the following. It often happens in thin-film work that t and $1/\mu$ are of the same order of magnitude and $A_{\theta 2\theta}$ has to be considered for a proper interpretation of the pattern. The μt product turns out to be a decisive quantity in the x-ray investigations of thin films.

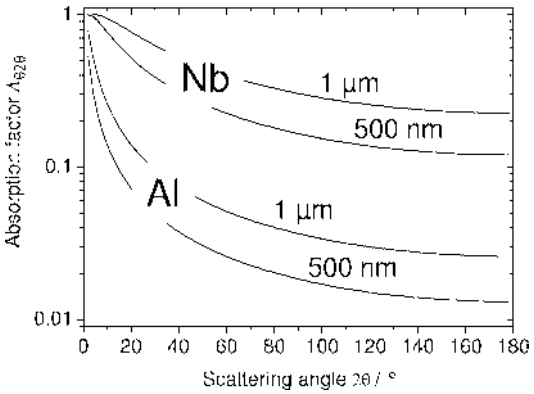


Figure 1.16 Absorption factor A for 500 nm and 1 μm thin Al and Nb films as function of 2θ.

1.3.8
Integration of the Interference Function

The central question of this section is now tackled regarding the integral intensity of a Bragg peak in a $\theta/2\theta$ scan. What we are interested in is the energy E that is received by the surface dS of the detector in the time element dt'

$$dE = I(\boldsymbol{R})dSdt' \tag{1.33}$$

The geometry of the quantities involved is shown in Fig. 1.17. If all the factors outlined above, i.e. square of the structure factor $|\boldsymbol{F_h}|^2$, multiplicity m, texture factor $T_{\boldsymbol{h}}$, geometry factor G, polarization factor $\overline{C^2}$ and absorption factor $A_{\theta 2\theta}$, are included into the intensity formula, the integration has to be done for

$$I(\boldsymbol{R})dSdt' = I_0 \frac{r_e^2}{R^2}\left|F_{\boldsymbol{h}}\right|^2 m_{\boldsymbol{h}} T_{\boldsymbol{h}} G\overline{C^2} \frac{A_{\theta 2\theta}(t)}{2\mu} \prod_{i=1}^{3} \frac{\sin^2\left(N_1 a\boldsymbol{Q}\boldsymbol{c}_i / 2\right)}{\left(a\boldsymbol{Q}\boldsymbol{c}_i / 2\right)^2} dSdt' \tag{1.34}$$

This expression is rather complex, but its main problem is related to the fact that the variables t' and S over which the integration has to be performed are not realized at first sight in the integrand. Therefore, the differential term has to be transformed to quantities over which the integration might be performed. For this purpose we aim at transforming dS and dt' to quantities that allow one to integrate over $(a\boldsymbol{Q}\boldsymbol{c_i})$ terms of the interference function. It is now assumed that the intensity of one single crystallite shall be estimated, while the corrections for the polycrystallinity of the sample shall be considered by multiplying by the factors given above. Without restricting the general validity of the derivation the crystallite is assumed to be (001) oriented and the reflection under consideration is of 00l type (see Fig. 1.17).

An important constraint in any x-ray scattering experiment is that the probing beam and the detected beam unavoidably exhibit a finite divergence δ. A divergence-free beam is a theoretical idealization that does not exist. Consequently, if the x-ray source and the detector are both at Bragg position θ_B one could still trace incoming and exiting beams that are off the diffraction position. The off-angle beams

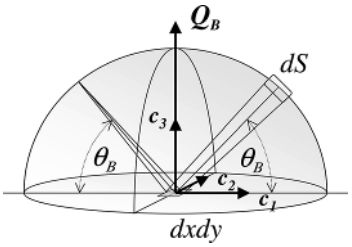


Figure 1.17 Geometrical quantities involved in the integration of the interference function.

exhibit diffraction angles of $\theta_B + \Delta\theta$. This also means in terms of the scattering vector that besides the ideal vector $\boldsymbol{Q}_B$ other $\boldsymbol{Q}$ vectors with $\boldsymbol{Q} = \boldsymbol{Q}_B + \Delta\boldsymbol{Q}$ would be operative at the Bragg position.

It is outlined in Instrumental Box 2 that a $\theta/2\theta$ scan may be carried out by rotating the sample by θ and the detector by 2θ. The detector thus rotates with a circular velocity of $d(\Delta\theta)/dt' = \dot{\theta}$ with respect to the sample which allows the first substitution to be made, namely $dt' = d(\Delta\theta)/\dot{\theta}$ and we obtain

$$dE = I(\boldsymbol{R})\frac{1}{\dot{\theta}}dSd(\Delta\theta) \tag{1.35}$$

The surface dS is proportional to the square of the sample–detector distance R. A small area $dxdy$ is illuminated on the sample surface by the incoming x-ray beam. This infinitesimally small area corresponds by

$$dS = R^2 \sin\theta dxdy \tag{1.36}$$

with the receiving area of the detector. The $\sin\theta$ term is simply caused by the tilt of the sample area when it is portrayed on the detector window. The illuminated area of the sample surface $dxdy$ depends on the divergence of the beam or on how strong $\Delta\boldsymbol{Q}$ deviates from $\boldsymbol{Q}_B$. The infinitesimal area element can thus be expressed by the scalar product of $\boldsymbol{Q}$ with the crystal lattice vectors $\boldsymbol{c}_1$ and $\boldsymbol{c}_2$ giving

$$dxdy = \left(\frac{\lambda}{4\pi\sin\theta}\right)^2 d(\boldsymbol{Q}\boldsymbol{c}_1)d(\boldsymbol{Q}\boldsymbol{c}_2) \tag{1.37}$$

The prefactor has to be introduced to normalize with respect to the length of $\boldsymbol{Q}$. The surface detector element can thus be expressed by the sample surface element according to

$$dS = \frac{R^2\lambda^2}{4a^2 4\pi^2 \sin\theta} d(a\boldsymbol{Q}\boldsymbol{c}_1)d(a\boldsymbol{Q}\boldsymbol{c}_2) \tag{1.38}$$

It should be noted that $\boldsymbol{Q}\boldsymbol{c}_1$ equals $\Delta\boldsymbol{Q}\boldsymbol{c}_1$, because the product of $\boldsymbol{Q}_B$ with $\boldsymbol{c}_1$ – and also $\boldsymbol{c}_2$ – yields zero under the assumed geometry. The integration over $d(a\boldsymbol{Q}\boldsymbol{c}_1)d(a\boldsymbol{Q}\boldsymbol{c}_2)$ is thus an integration in the vicinity of the Bragg reflection.

The transformation from $d(\Delta\theta)$ to $d(a\boldsymbol{Q}\boldsymbol{c}_3)$ can be obtained by the derivative of the latter quantity with respect to the first. For this purpose the decomposition $\theta = \theta_B + \Delta\theta$ is applied

$$\frac{d(\boldsymbol{Q}\boldsymbol{c}_3)}{d(\Delta\theta)} = \frac{d}{d(\Delta\theta)}\frac{4\pi\sin(\theta_B + \Delta\theta)}{\lambda} = \frac{4\pi\cos\theta}{\lambda} \tag{1.39}$$

Finally, the differentials are adopted to the arguments in the denominator and one arrives at

$$\frac{dS}{R^2}d(\Delta\theta) = \frac{\lambda^3}{4a^3(2\pi)^3\sin 2\theta}\prod_{i=1}^{3} d\left(a\boldsymbol{Q}\boldsymbol{c}_i\right) \tag{1.40}$$

Instrumental Box 2:

Generation of X-rays by X-ray Tubes

X-rays are generated when electrons with kinetic energies in the keV range and above impinge on matter. The emission spectrum comprises a continuous part, called Bremsstrahlung, and some discrete lines indicative of the chemical elements of the target material. In laboratory x-ray tubes electrons are accelerated onto an anode plate made from a specific metal of high purity. The cross-section of such a tube is shown in Fig. i1.1. The electrons are emitted from the cathode filament and accelerated towards the anode plate. The anode is typically fabricated from copper, chromium, molybdenum or another metal as listed in Table i1.1. The electron current between filament and anode may be adjusted by tuning the filament current in the range of some 10 mA. When impinging upon the anode the electrons are decelerated by their interaction with the target plate atoms leading to the emission of x-rays. The acceleration voltage (in kV) must be greater than the energy of the characteristic radiation required by the experiment (in keV). Energy E and wavelength λ of the radiation are related by

$$E\ [\mathrm{keV}] = 1.2398 \Big/ \lambda\ [\mathrm{nm}] \qquad \text{(i2.1)}$$

As a rule of a thumb line energies may be converted to wavelengths by relating them to the set point 11.1 keV ≈ 0.111 nm. This relation is precise to 0.6% and may easier be remembered than Eq. (i2.1). Often the anode is made of copper to make use of the characteristic Cu Kα line. The Cu Kα wavelength is 0.154 nm which is adequate to 8.04 keV. Other x-ray tubes may be used if the diffraction pattern has to be contracted or expanded or if the excitation of x-ray fluorescence from the sample is to be avoided. A prominent example for the latter effect is given by Fe-containing samples that cause a strong background when Cu Kα radiation is applied.

Table i2.1 Metals used as anodes of x-ray tubes with characteristic wavelengths λ, typical Kβ filter materials and their appropriate K-edge wavelengths λ_K.[a]

Target element	Z	λ (nm)				Kβ filter	λ_K (nm)
		Kα_1	Kα_2	K$\bar{\alpha}$	Kβ_1		
Cr	24	0.228975	0.229365	0.22909	0.20849	V	0.2269
Fe	26	0.193631	0.194002	0.19373	0.17567	Mn	0.1896
Co	27	0.178900	0.179289	0.17905	0.16208	Fe	0.1744
Ni	28	0.165794	0.166178	0.16591	0.15002	Co	0.1608
Cu	29	0.154059	0.154441	0.15418	0.139225	Ni	0.1488
Mo	42	0.709317	0.713607	0.7107	0.63230	Zr	0.6889
Ag	47	0.559422	0.563813	0.5608	0.49708	Rh	0.5339

a From various tables of the *International Tables for Crystallography*, Vol. C, Section 4.2.2.

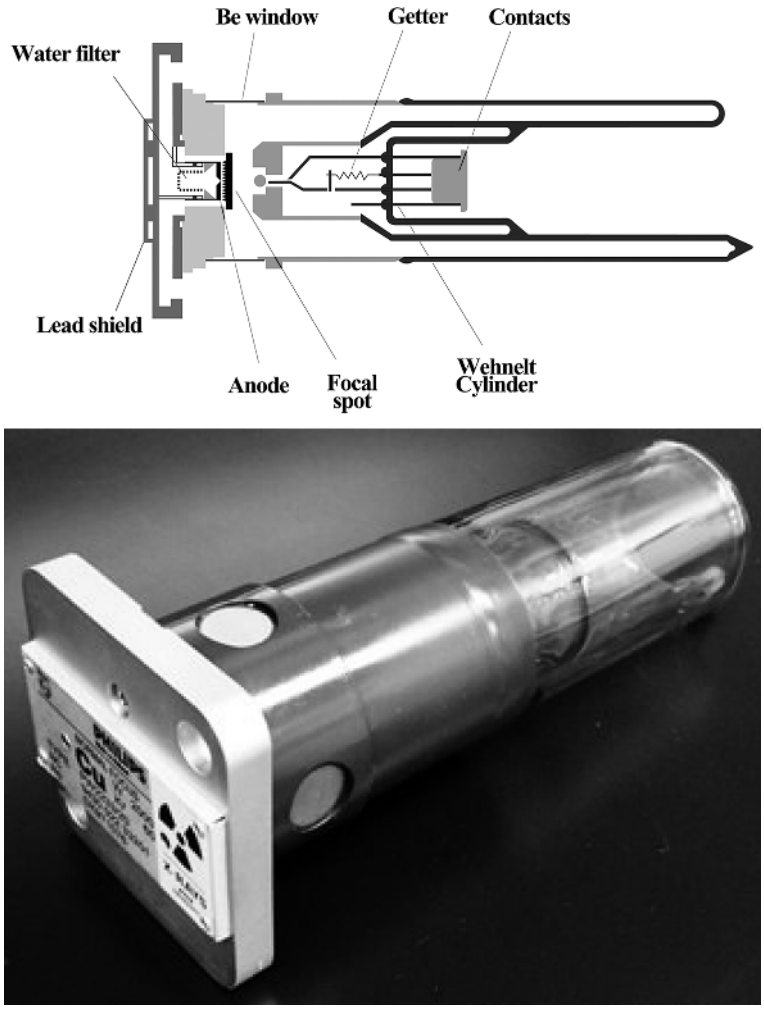


Figure i2.1 Schematics and photographs of laboratory x-ray tubes. This page: conventional x-ray tube type. Next page: ceramic x-ray tube for less laborious change from line to point focus mode and vice versa. (Kindly provided by PANalytical.)

The process of impact ionization and relaxation of an x-ray emitting atom is shown schematically in Fig. i2.2. In this sequence of processes, bound electrons are first released and subsequently an electron from a higher energy level relaxes into the emptied state. The relaxation is associated with the emission of radiation the energy of which corresponds to the energy difference between the final and initial state. This energy thus sensitively depends upon the chemical nature of the emitting atom. According to the levels involved the relaxation of the emitted radiation is denoted by $K\alpha_1$, $K\beta_2$, $L\alpha$, etc. In most x-ray scattering experiments only the characteristic emission lines are of interest.

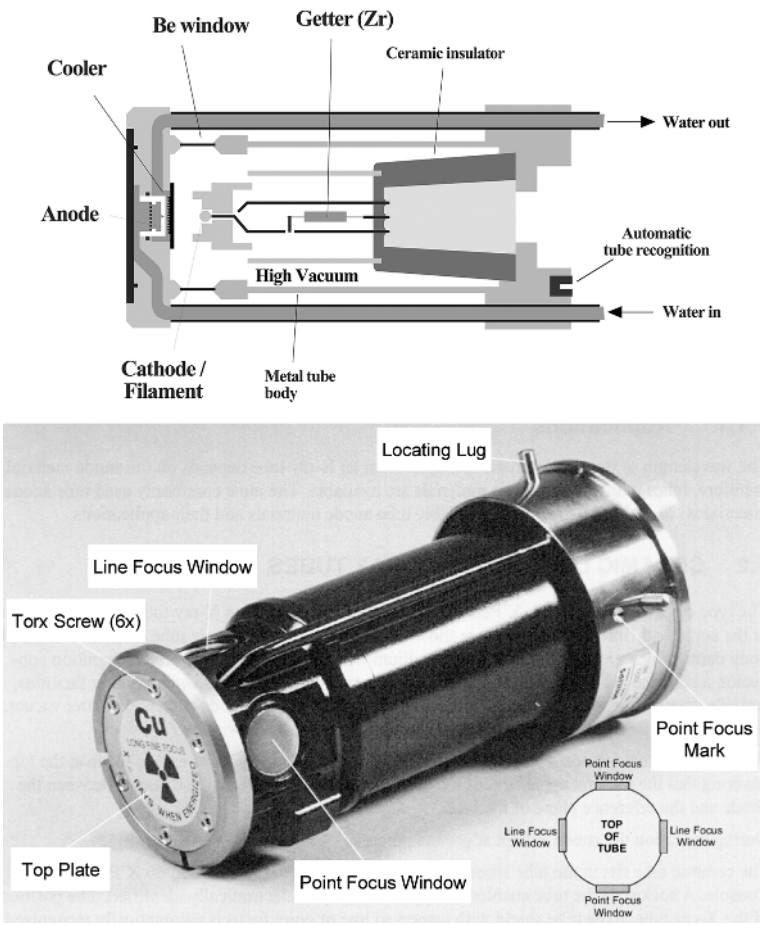


Figure i2.1 continued

In the majority of cases investigations are performed with Kα radiation, because of its higher intensity compared to Kβ. A closer look at the *K*α radiation reveals its doublet nature. The doublet resolution increases for Bragg peaks with increasing scattering angle 2θ. Moreover, the occurrence of the splitting strongly depends on the microstructure of the sample, and in many polycrystalline thin-film investigations the α_1–α_2 splitting may not be observed. In such cases the weighted average of both lines is used denoted by $K\bar{\alpha}$ or simply Kα. The Kβ line may severely disturb the interpretation of the diffraction pattern and various techniques are applied for its suppression. Very common are edge filters that are introduced into the incident beam path and make use of the fact that the photoionization of deep levels requires a certain minimum energy. In the case of copper, $E(\text{Cu K}\beta_1) = 8.9$ keV and thus a thin Ni foil can be used as an edge filter that significantly

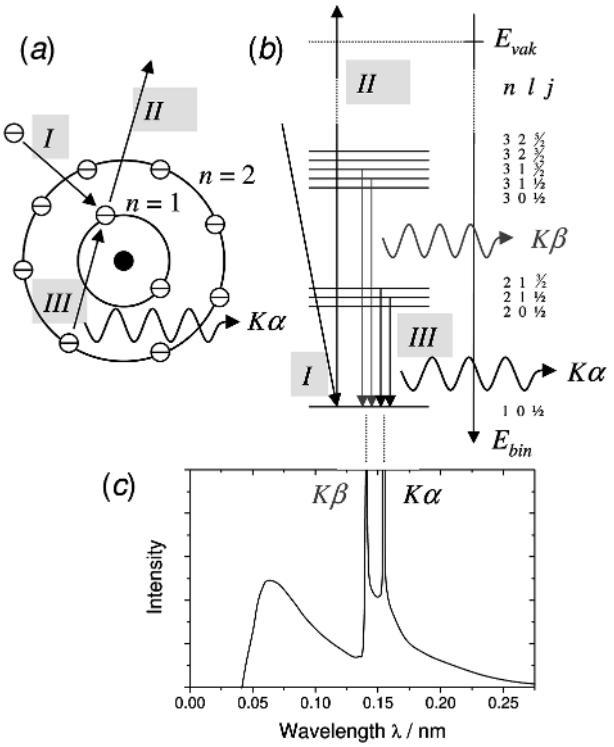


Figure i2.2 (a) Emission of x-rays by an atom through sequential processes of electron impact (I), ionization (II) and simultaneous electronic relaxation and emission of radiation (III). (b) Elementary processes visualized in the term scheme, where only transitions that obey the selection rules $\Delta l = \pm 1$ and $\Delta j = 0, \pm 1$ are shown. (c) Schematic x-ray spectrum emitted by an anode. It is composed of a continuous Bremsstrahlung background and discrete single lines.

suppresses the Kβ line (see Exercise 1.14). Other foil materials for other tubes are specified in Table i2.1.

The filament and anode operate in a high-vacuum environment of the sealed tube. The decoupling of radiation is facilitated via one of the four Be windows (300 μm thickness) at each side of the tube. The dimensions of the focal-spot size on the anode plate range between (0.4 × 10) mm and (2 × 12) mm. The anode focus is "seen" by the sample under a take-off angle between 2° and 6°. The focus either appears as a line or a spot according to which window is used for the decoupling. The x-ray tube may thus be operated in line focus mode or point focus mode depending on the experimental necessities. Remember that the point focus is not a point focus, but a line focus viewed from the side (see Fig. i.1.3). Due to the high power dissipation at the focal spot the back of the anode plate is water cooled.

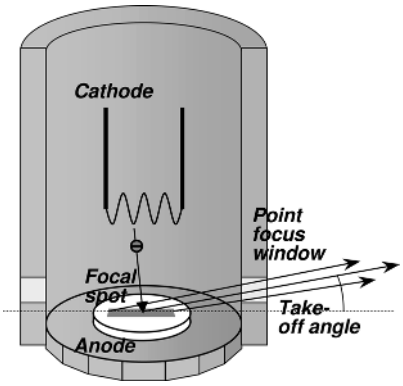


Figure i2.3 Schematic of x-ray tube head to visualize point focus operation.

In addition to the sealed x-ray tubes discussed above, so-called rotating anode x-ray generating systems are also in use. These make use of an improved dissipation of the heat introduced by impinging electron current on the anode by rotating it. Higher emission rates of x-rays by a factor of about 3–5 may be obtained. Orders of magnitude higher radiation intensities are available at synchrotron beamlines.

The factor in front of the differential product is called the Lorentz factor L. Frequently, only the term $L = 1/\sin 2\theta$ is denoted as the Lorentz factor. Its effect on the course of intensity in conjunction with the geometry factor G and the polarization factor $\overline{C^2}$ is depicted in Fig. 1.14.

Inserting the transformation Eq. (1.40) into the differential form for the energy received by the detector

$$I(\boldsymbol{R})dSd(\Delta\theta) = I_0 \frac{r_e^2}{R^2\dot{\theta}} \left|F_{\boldsymbol{h}}\right|^2 m_{\boldsymbol{h}} T_{\boldsymbol{h}} G\overline{C^2} \frac{A_{\theta 2\theta}(t)}{2\mu} \prod_{i=1}^{3} \frac{\sin^2\left(N_i a\boldsymbol{Q}\boldsymbol{c}_i/2\right)}{\left(a\boldsymbol{Q}\boldsymbol{c}_i/2\right)^2} dSd(\Delta\theta) \tag{1.41}$$

the integration may be carried out and is found to yield

$$\iiint \prod_{i=1}^{3} \frac{\sin^2\left(N_i a\boldsymbol{Q}\boldsymbol{c}_i/2\right)}{\left(a\boldsymbol{Q}\boldsymbol{c}_i/2\right)^2} d\left(a\boldsymbol{Q}\boldsymbol{c}_i/2\right) = N_1 N_2 N_3 \tag{1.42}$$

The three integers N_i give the length of the crystallite in units of cell edges and are related to the volume of the sample V and the unit cell V_{uc} by

$$N_1 N_2 N_3 = \frac{V}{a^3} = \frac{V}{V_{uc}} \tag{1.43}$$

If the substitution of V_{uc} for a^3 is also performed for the Lorentz factor and the other results from above are applied we finally end up with the expression for the integral intensity of a Bragg reflection in a $\theta/2\theta$ scan

$$I_{\boldsymbol{h}} = I_0 \frac{r_e^2}{\dot{\theta}} \lambda^3 m_{\boldsymbol{h}} T_{\boldsymbol{h}} \frac{1+\cos^2\theta}{\sin\theta \sin 2\theta} \frac{\left|F_{\boldsymbol{h}}\right|^2}{V_{\mathrm{uc}}^2} V \frac{A_{\theta 2\theta}(t)}{2\mu} \tag{1.44}$$

Various points concerning the integral intensity Eq. (1.44) are of interest. Firstly, it is realized that the intensity is proportional to $|F_h|^2/V_{uc}^2$. This ratio has the character of a squared electron density and underlines again the statement made above that x-ray diffraction patterns scale with the square electron density $\rho_e{}^2$ of the sample. Secondly, there are various factors active that may cause a severe reduction of intensity with increasing scattering angle 2θ. The ratio of trigonometric functions occurring in Eq. (1.44) has already been plotted in Fig. 1.14 and can be seen to reduce the integral intensity of a reflection by an order of magnitude, depending on where it occurs. Also the structure factor ceases strongly as a function of 2θ and even more so for the square of it. A special feature in thin-film analysis is the damping caused by the absorption factor $A_{\theta 2\theta}(t)$ which also increases with increasing scattering angle. The different factors make comprehensible the features of the thin Al film diffraction pattern shown in Fig. 1.10.

In the majority of investigations the integral intensity is specified by virtue of a scaling factor SCF that lumps together all instrumental settings like scan velocity $\dot{\theta}$, slit width, etc., and allows the comparison of integral intensities from one diffraction pattern on a relative scale

$$I_{\boldsymbol{h}} = \mathrm{SCF} \cdot m_{\boldsymbol{h}} \cdot T_{\boldsymbol{h}} \cdot Lp \cdot \left|F_{\boldsymbol{h}}\right|^2 \cdot A_{\theta 2\theta}(t) \tag{1.45}$$

The convention is also often used to abbreviate the product of Lorentz, geometry and polarization factor by $Lp = G\overline{C^2}L$ and denoting it as the Lorentz-polarization factor.

In practice, it may be a reliable rule of a thumb in thin-film work to extend the $\theta/2\theta$ scan to $2\theta_{\max} = 60°$ to 80° when Cu Kα radiation is used while higher 2θ angles are associated with too low a signal-to-noise ratio. The use of Cu Kα radiation with $\lambda = 0.154$ nm is widespread for the investigation of inorganic layers because it portrays interplanar spacings d from 0.355 to 0.154 nm into a 2θ range of 25–60°. However, the rule should only be taken as a recommendation and not as dogma. In any case, the analyst should check the range of scattering angles useful for the material and the analytical question under investigation. As a first step it might be helpful to calculate the strength of the μt product and hence the course of $A_{\theta 2\theta}(t)$ if the thin film thickness and composition – or reasonable estimates – are available.

An important point regarding the integral intensity of an x-ray reflection has to be mentioned. If the measurement is not made with a polycrystalline thin film, but with a single crystalline material a modification of Eq. (1.44) might become necessary. In highly perfect single crystals it may happen that the incoming beam is diffracted twice or even multiple times, which can effectively cause an attenuation of the reflection much stronger than accounted for by the absorption factor given above. The calculation of the diffracted intensity then has to take into account all wave fields that propagate in the crystal. The description of these phenomena is fa-

cilitated within the framework of the dynamical theory of x-ray diffraction, while the considerations outlined above are denoted as kinematical theory. For many applications the results of the kinematical theory as condensed in Eq. (1.44) are sufficient to explain the diffraction pattern of thin films – at least if polycrystalline layers are concerned. Solely in high-resolution work with epitaxial layers the dynamical theory sometimes has to be applied as is outlined in Chapter 8.

1.4 Applications

Metals have found applications in thin-film technology due to their luster and high electrical conductivity. Both properties are caused by the high mobility of electronic charge carriers in the crystal lattice. Decorative and anticorrosion coatings of chromium, zinc and derivative alloys for armatures, metal work, kitchen fittings, automotive parts, etc., are mostly deposited by electroplating. The technique of gilding of jewelry, porcelain, relics, etc., by gold leaf of only micrometers in thickness has been continuously developed for more than 4000 years. Typical modern applications of thin metal films are Al layers of less than 100 nm thickness used as barrier coatings on food packaging and as reflective coatings in light housings for automobile headlights to mention only a few examples.

Laterally structured thin metal films also play an enormous role in the semiconductor industry as electrical contacts between micrometer- and even submicrometer-sized devices. For this purpose, metals are deposited by electroplating, chemical or physical vapor deposition and subsequently structured by lithographic procedures to yield conducting plain contacts and metal level connecting vias. Al plays a vital role in these applications, but a severe problem that has to be addressed for metallic interconnects is electromigration limiting the mean time to failure of integrated circuits. Due to its higher electrical conductivity, Cu has recently partly replaced Al, as depicted in Fig. 1.18 where the highly complex three-dimensional stacking of Cu layers is shown [2]. Cu films deposited by electroplating were found to exhibit a remarkable microstructural evolution after plating [3]. Among the microstructural properties of interest in Cu interconnects are the texture and grain size [4] that can both affect the electromigration resistance. It should be mentioned, however, that the introduction of Cu in the Si industry has been avoided for a long time, because Cu is an extremely fast diffuser in Si and may severely degrade integrated circuit performance by acting as a deep-level recombination center. The diffusion of Cu into the semiconductor has to be safely prohibited by introducing anti-diffusion barriers, the functionality of which has been effectively investigated using x-ray diffraction procedures enabling their optimization [5].

Thin metal films are also of interest because of their mechanical properties and various basic investigations have been performed with x-ray diffraction techniques due to their model character for thin-film systems in general. Refractory Nb films, for instance, are qualified by the high yield strength of Nb for engineering applications and were found to exhibit pronounced depth dependencies during growth

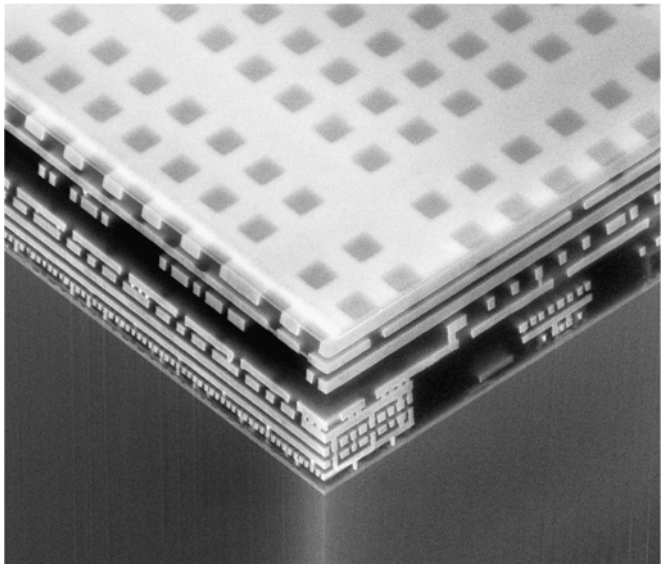


Figure 1.18 Thin film metallic interconnect structure as used in a modern microelectronic chip. The multilayer system exhibits a total thickness in the μm range (figure kindly provided by AMD, Dresden [2]).

[6]. The same phenomenon was identified for titanium films that are applied as adhesion layers for hard coating applications [7]. Increasing attention has been paid in recent years to the interesting plastic properties of nanocrystalline metals. For instance, plastic deformations in electroplated nanocrystalline Ni films could be revealed by *in situ* investigations to be reversible upon unloading instead of producing a residual dislocation network [8]. X-ray scattering investigations of thin metal films are used extensively to investigate grain sizes, crystalline lattice faults, texture and residual stress. The various x-ray scattering techniques to elucidate these microstructural features are outlined in the following chapters.

Exercises

1.1 The determination of the classical radius of the electron proceeds by assuming that the total electric field energy $\int \boldsymbol{D} \cdot \boldsymbol{E} dV$ is confined to the space surrounding the spherical particle of radius r_e. Show that $r_e = e^2/(4\pi\varepsilon_0 mc^2)$ is obtained when the total field energy is identified with the energy of the rest mass mc^2.

1.2 Consider a preferably plane transparent thin film on a reflecting substrate (like a Si wafer). Examine it in daylight and in a room illuminated by neon light. Which optical phenomena can be observed in both cases? Why is the optical length of coherence longer in one case than in the other? How does the coherence length depends on the frequency spectrum of the radiation?

1.3 What is the momentum of an 8 keV x-ray photon? Compare this to the average momentum of an Ar gas atom confined to a vessel under thermodynamic standard conditions.

1.4 Give the general expression for $1/d_{hkl}^2$ (Table 1.1) for the triclinic crystal by starting from $1/d_{hkl}^2 = (h\boldsymbol{b}_1 + k\boldsymbol{b}_2 + l\boldsymbol{b}_3)^2$, with the reciprocal lattice vectors $\boldsymbol{b}_i$ depending like $\boldsymbol{b}_i = (\boldsymbol{a}_j \times \boldsymbol{a}_k)/(\boldsymbol{a}_i\,(\boldsymbol{a}_j \times \boldsymbol{a}_k))$ on the unit cell vectors $\boldsymbol{a}_i$.

1.5 Show that the summation over all scattering centers according to Eq. (1.9) indeed yields Eq. (1.10). Make use of the geometrical sum.

1.6 Derive the atomic form factor of He by modeling it with the spherical charge distribution of two electrons $\rho(r) = (2e/\pi)(2/a_0^3)\exp(-4r/a_0)$ and performing the integration (1.17). Find a numerical approximation in the form of eq. (1.18) through a non-linear regression. What is the precision of the fit in the $\sin\theta/\lambda$ range from 0 to 10 nm^{-1} when the numerical value for Bohr's radius $a_0 = 0.0529$ nm is inserted?

1.7 Derive the structure factor $\boldsymbol{F}_h$ and extinction conditions of the three lattice types bcc, fcc, hcp from the general expression (1.23). Show that the evaluation of an expression comparable to Eq. (1.9) for the bcc lattice yields an equivalent result.

1.8 What are the multiplicities m_h of Bragg peaks of the thin Al film shown in Fig. 1.10?

1.9 Suppose a Bragg reflection in a $\theta/2\theta$ pattern to be observed at $2\theta_1$ when Cu Kα_1 monochromatized radiation is applied. What would be the appropriate position of $2\theta_2$ for the Cu Kα_2 line? In absolute values for $2\theta_1 = 32°$?

1.10 A diffractometer is run without suppression of Kβ radiation. Where do the β peaks occur in the diffraction pattern compared to the α peaks? General: are the interference lines of higher energy radiation shifted towards lower or higher scattering angles 2θ?

1.11 Calculate the c/a ratios for the hcp-structured metals given in Table s1.1. How do they deviate from the "ideal" value of 1.633 and what is the meaning for the two different interatomic distances d_1 and d_2 in the hcp structure?

1.12 Determine the distance d of an atom in the fcc and bcc structure to its nearest neighbors as a function of the lattice parameter a. Do the same for the hcp structure for interatomic distances within the basal plane and in the out-of-

plane direction. Assume that atoms may be modeled by spheres and calculate the volume ratio of space occupied by spherical atoms V_{at} and the complete unit cell volume V_{uc} for all three structure types.

1.13 Calculate the linear attenuation coefficient μ and the penetration depth $\tau_{1/e}$ for Be, Zn, Fe, Ag and Au for irradiation with Cu Kα radiation (8.04 keV). Determine the density and mass attenuation coefficient of the materials from tables like Table 2.1 or from the internet.

1.14 The mass absorption coefficients for Cu Kα and Cu $K\beta_1$ radiation in Ni are 48.8 and 279 $cm^2\ g^{-1}$ while the mass density of Ni is 8.9 $g\,cm^3$. Calculate the intensity ratios $I(K\alpha)/I(K\beta_1)$ and $I(K\alpha)/I_0(K\alpha)$ after Cu K radiation with an initial ratio $I_0(K\alpha)/I_0(K\beta_1)$ of 3:1 has been transmitted through a Ni foil of (a) 8, (b) 15 and (c) 20 µm thickness. Which of these foils would you consider as the optimum Kβ filter?

1.15 In cubic substances two group of lattice planes may scatter simultaneously for the same scattering angle 2θ, because $d_{hkl} = \sqrt{h^2 + k^2 + l^2}\,/\,a$ is not a one-to-one unique function of Miller indices *hkl*. Which are the first double reflections to occur in a $\theta/2\theta$ scan? Give the first three of them for fcc and bcc structures.

1.16 An x-ray copper tube is operated with 40 kV and 40 mA and is assumed to have efficiency for x-ray generation of 1%. X-rays are emitted with $\cos^2$ characteristic and the take-off angle is 6°. The divergence slit is 1°. By how many x-ray photons is the sample irradiated per second? How many Cu Kα photons? Give order of magnitude estimations.

1.17 What is the varied measurement quantity in all kinds of spectrometers and why is it inadequate to denote a diffractometer as a spectrometer? The same arguments are valid in distinguishing a diffraction pattern from a spectrum.

1.18 Derive the dependence of the radius of the focusing circle R_{FC} on the diffraction angle θ and goniometer radius R.

1.19 The element Polonium has only found few technical applications, since its isotopes are all unstable with the most long-living ones decaying under emission of α particles. The most relevant application of Po is as initiator in nuclear fission bombs. Devices based on uranium, for instance, operate by the gun principle and comprise two undercritical U masses that are shot into each other for ignition. The chain reaction of fission processes is reported to be accelerated by covering one of the masses with Po and the other by Be. The α particles emitted from Po are then captured by Be nuclei leading to higher Be isotopes that act as neutron emitters accelerating the U fission reaction. About 2×10^4 nuclear weapons with the explosive power of more than 10^6 Hiroshima bombs are still stored in the arsenals of the atomic powers although they pledged in the Non-Proliferation Treaty of 1970 ''to pursue negotiations in good faith on effective measures relating to cessation of the nuclear arms race at an early date and to nuclear disarmament, and on a Treaty on general and complete disarmament under strict and effective international control'' (Article VI). Various organizations exists, in which scientists are acting for disarmament and the abolition of nuclear weapons like the International Network of Scientists and Engineers for Global Responsibility (www.inesglob-

al.com), the Pugwash movement (pugwash.org), the Union of Concerned Scientists (ucsusa.org) and others. Visit the internet sites of these organizations and evaluate what scientists can do to assure the humane and useful application of their work.

References

Monographs relevant to this chapter

B. E. Warren, *X-Ray Diffraction,* Addison-Wesley, Reading, MA, 1969.
B. D. Cullity, *Elements of X-Ray Diffraction,* Addison-Wesley, Reading, MA, 1967.

Special papers

[1] E. N. Maslen, A. G. Fox, M. A. O'Keefe, X-ray Scattering, in: E. Prince (Ed), *International Tables for Crystallography*, Vol. C (Kluwer Academic, Dordrecht, 2004), p. 554.
[2] M. A. Meyer & E. Zschech, AMD, Dresden (2004).
[3] J. M. E. Harper, C. Cabral, P. C. Andricacos, L. Gignac, I. C. Noyan, K. P. Rodbell, C. K. Hu, Mechanism for microstructure evolution in electroplated copper thin films near room temperature, *J. Appl. Phys.* **86** (1999) 2516.
[4] C. Lingk, M. E. Gross, W. L. Brown, X-ray diffraction pole figure evidence for (111) sidewall texture of electroplated Cu in submicron damascene trenches, *Appl. Phys. Lett.* **74** (1999) 682.
[5] Y. S. Gong, J.-C. Lin, C. Lee, Interdiffusion and reactions in the Cu/TiN/Si thin film system, *Appl. Surf. Sci.* **92** (1995) 335.
[6] B. Okolo, P. Lamparter, U. Welzel, E. J. Mittemeijer, Stress, texture, and microstructure in niobium thin films sputter deposited onto amorphous substrates, *J. Appl. Phys.* **95** (2004) 466.
[7] M. Birkholz, C. Genzel, T. Jung, X-ray diffraction study on residual stress and preferred orientation in thin titanium films subjected to a high ion flux during deposition, *J. Appl. Phys.* **96** (2004) 7202.
[8] Z. Budrovic, H. Van Swygenhoven, P. M. Derlet, S. Van Petegem, B. Schmitt, Plastic Deformation with Reversible Peak Broadening in Nanocrystalline Nickel, *Science* **304** (2004) 273.